THE JOURNAL OF PHYSICAL CHEMISTRY A
A JOURNAL OF THE AMERICAN CHEMICAL SOCIETY

pubs.acs.org/JPCA Article

Effect of Cations on the Oxidation and Atmospheric Corrosion of Iron Interfaces to Minerals

Chathura de Alwis, Mikhail Trought, Julia Lundeen, and Kathryn A. Perrine*

Cite This: *J. Phys. Chem. A* 2021, 125, 8047–8063 Read Online

ABSTRACT: Surface corrosion involves a series of redox reactions that are catalyzed by the presence of ions. On infrastructure surfaces and in complex and natural environments, iron surfaces readily undergo redox reactions, impacting chemical processes. In this study, the effect of how cations influence the formation of the mineral scale on iron surfaces and its connection to surface corrosion was investigated in $CaCl_2$(aq) and NaCl(aq) electrolytes. Polarized modulated-infrared reflection absorption spectroscopy (PM-IRRAS) measurements were used to measure the oxidation and formation of carbonates at the air/electrolyte/iron interface, which confirmed that the iron surface oxidized faster in $CaCl_2$(aq) than in NaCl(aq). PM-IRRAS, attenuated total reflectance–Fourier transformed infrared spectroscopy, and X-ray photoelectron spectroscopy show that after the adsorption of atmospheric O_2 and CO_2, calcium carbonate ($CaCO_3$) in the form of calcite and aragonite was produced on iron in the presence of $CaCl_2$(aq), whereas siderite ($FeCO_3$) was produced on the surface of iron in the presence of NaCl(aq). However, in either solution without gradual O_2 and CO_2 exposure, a heterogeneous mixture of lepidocrocite (γ-FeOOH) and an iron hydroxy carbonate ($Fe_x(OH)_yCO_3$) was grown on the iron surface. *In situ* liquid AFM was used to measure the surface roughness in $CaCl_2$(aq) and NaCl(aq), as an estimation of the corrosion rate. In $CaCl_2$(aq), Fe was found to corrode faster than Fe in NaCl(aq) due to more ions at equimolar concentrations. Surface physical changes, as measured by *ex situ* AFM, confirmed the presence of a heterogeneous mixture of γ-FeOOH and an $Fe_x(OH)_yCO_3$ in the submerged region. This indicates that the cation does not affect the type of mineral grown on the Fe surface in the region completely submerged in the electrolyte. These results suggest that the cations play a unique role in the initial stages of corrosion at the interface region, influencing the uptake of atmospheric CO_2 and mineral nucleation. The knowledge gained from these interfacial reactions are important for understanding the connection between surface corrosion, mineral grown, and CO_2 capture for sequestration.

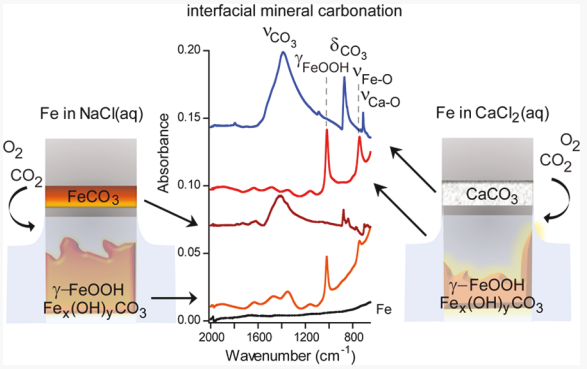

1. INTRODUCTION

Corrosion is a natural process where metals are oxidized from exposure to humidity and oxidizing gases. Corrosion impacts industrial infrastructure affecting water quality and material degradation, due to the breakdown of metal protective coatings within municipal pipes leading to severe health hazards, as was observed in the Flint water crisis.[1−3] Municipal water lines undergo corrosion from spontaneous electrochemical reactions and buildup layers of the inorganic scale on the surface.[4] These scale films are produced from exposure to hard water, consisting of sulfates, carbonates, bicarbonates, and phosphates of calcium and magnesium. The growth of scale films on the internal walls acts as a physical barrier between aqueous solutions and the metal pipeline, preventing particulate dissolution into municipal water lines.[5−9] However, there are still gaps into how the chemistry of these complex mixtures influences the mechanism of corrosion and scale formation.

Inorganic thin films are a complex mixture of minerals produced on the surface of metals from corrosion and other complex mechanisms.[9,10] The chemical composition of the mineral depends upon the metal and the chemical composition of solutions, solution pH, temperature, and gases in the environment.[11−13] Atmospheric dust and other particulate matter that settle on metal surfaces can also lead to corrosion, such as in the crevice phenomenon, where the small space between dust and the surface of the corroding species traps water easily, and fluctuations in relative humidity cause dissolved ions to deposit onto the surface of the substrate, increasing corrosion rates.[2,14] Corrosion reactions and mineral formation are complex in nature as gases and ions in electrolytes come in contact with metal surfaces, producing oxides, hydroxides, and carbonates.[15−19]

Received: July 20, 2021
Revised: August 16, 2021
Published: September 7, 2021

https://doi.org/10.1021/acs.jpca.1c06451
J. Phys. Chem. A 2021, 125, 8047–8063

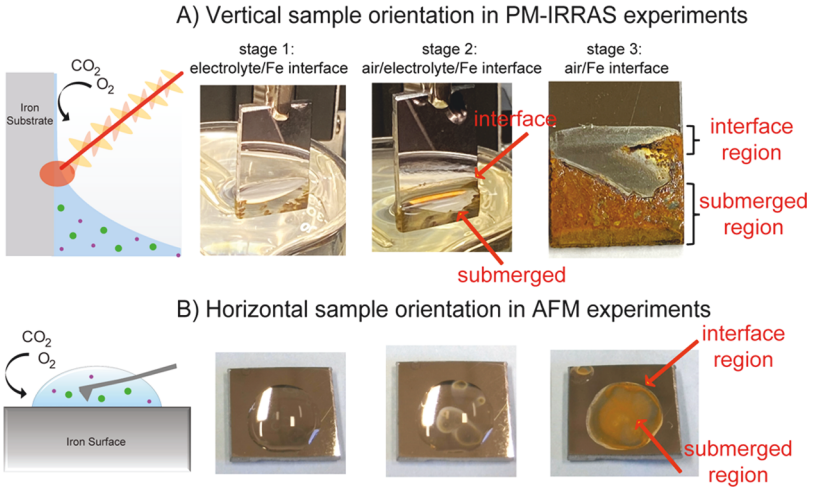

Figure 1. Sample orientation for the (A) PM-IRRAS experiments (vertical orientation) and (B) AFM experiments (horizontal orientation).

The mechanism of corrosion begins with pitting of the surface with typically chloride ions, leading to breakdown of the native oxide surface layers, dissolution of the metal surface (acting as the anode), followed by metal oxidation, and results in the growth of inorganic mineral scale.[11,20] The chemical composition of these minerals are influenced by the type of ions present in aqueous solutions and exposure to oxidizing gases, such as oxygen, water, and carbon dioxide.[21−25] The presence of ions, particularly chloride,[26] is known to accelerate or catalyze the corrosion, due to increased ionic strength affecting charge transfer in the redox reaction.

Iron interfaces are ideal for studying fundamental corrosion processes as they comprise not only material infrastructure but also soils and atmospheric dust present in the mineral cycle, which undergo spontaneous redox reactions in aqueous ambient environments.[27−31] Although there are many studies pertaining to the corrosion process of iron,[6,32−34] there are few studies connecting how the chemistry in complex mixtures from ions, gases, and solid surfaces impacts surface corrosion, chemistry, and mineral growth. Our previous studies have shown that siderite ($FeCO_3$) is produced from exposure of Fe to aqueous NaCl(aq) and atmospheric CO_2.[13] In HCl(aq), lepidocrocite (γ-FeOOH) was produced at the iron interface, suggesting that only O_2 from air exposure influenced the mineral product. These studies show that at the iron interface, distinct minerals were formed in a complex environment of chlorinated electrolytes and air exposure and that polarized modulated-infrared reflection absorption spectroscopy (PM-IRRAS) is used to monitor the vibrational signatures during the formation of the minerals at the air/electrolyte/solid interface.

The objectives of this study were to measure how the cation affects the corrosion and oxidation of Fe interfaces to mineral films. A surface chemistry approach in three stages was used to investigate the surface mechanism and changes at the air/electrolyte/iron interface and in solution. These three stages are (1) the Fe surface in the electrolyte solution, (2) the air adsorption stage where the electrolyte solution is gradually removed to allow for exposure of the liquid/iron interface to atmospheric O_2 and CO_2, and (3) the oxidation stage, where the electrolyte was completely removed, allowing complete oxidation at the air/iron interface. We investigated two different chloride electrolytes, NaCl(aq) and $CaCl_2$(aq), using PM-IRRAS to measure the interfacial oxidation and formation of minerals. The chemical compositions of the corrosion products on iron at the interfacial area and the region submerged in solution were compared using X-ray photoelectron spectroscopy (XPS) and attenuated total reflectance−Fourier transform infrared (ATR−FTIR) spectroscopy. *In situ* liquid atomic force microscopy (AFM) was used to estimate the corrosion rates by imaging and measuring surface roughness in solution as a function of time. The resulting surface topography of mineral growth was measured using *ex situ* AFM after air oxidation. This approach allows us to measure different stages in the corrosion mechanism, from the initial stages in solution using liquid AFM, surface oxidation during air exposure for O_2 and CO_2 using PM-IRRAS, and post analysis using FTIR, XPS, and AFM. Our results suggest that the presence of the countercation at the air/electrolyte/iron interface highly influence the mineral formation. These studies ultimately connect mechanistic processes of corrosion in complex environments, from gases and electrolytes to nucleation and growth of minerals.

2. METHODS

2.1. Sample Preparation. *2.1.1. Surface Preparation.* Two grades of iron metals were used for the experiment. Metal iron (iron(II), 99.99%, Allied Metals Corp. and Puratronic, 99.995% metals basis, Alfa Aesar) was obtained in the form of a metal plate and cut into small sample pieces (2.0 cm × 1.0 cm × 0.20 cm). One side of each sample was polished using a metal polishing instrument (Struers, LaboPol-1) in a four-step metal polishing method as described previously[13] to a mirror finish. This was necessary to produce a highly reflective surface for PM-IRRAS measurements and a defect-free surface for AFM measurements. The samples along with their molds were rinsed with distilled water to remove the remaining particulate matter coming from the polishing material after every polishing step. The polished sample along with its supporting mold was sonicated for 5 min in ethanol to remove impurities. Polished metal iron samples were ejected out of the plastic mold by pressing hard through a vice. The polished iron samples were cleaned with Micrell soap solution followed by nanopure water (18.2 MΩ cm, Millipore Inc.) to remove the soap and finally sonicated in ethanol for 15 min.

2.1.2. Solution Preparation. A 100 mM NaCl(aq) stock solution was prepared using NaCl (99.0%, Sigma-Aldrich) and

https://doi.org/10.1021/acs.jpca.1c06451
J. Phys. Chem. A 2021, 125, 8047−8063

nanopure water (18.2 MΩ cm, Millipore Inc.). A stock solution of $CaCl_2$(aq) of 50 mM concentration was prepared using anhydrous $CaCl_2$ (>96.0%, Sigma-Aldrich). All the PM-IRRAS corrosion studies were carried out with 10 mM concentrations of NaCl(aq) and $CaCl_2$(aq) solutions by suitably diluting these stock solutions in a 50 mL beaker. For AFM imaging experiments, dilute concentrations of each electrolyte were required to slow down corrosion to observe it on a slower time scale. Therefore, a stock solution of 10 mM NaCl(aq) solution was prepared using NaCl (99.0%, Sigma-Aldrich), and a 10 mM $CaCl_2$ (aq) solution was prepared using anhydrous $CaCl_2$ (>96.0%, Sigma-Aldrich) using nanopure water (18.2 MΩ cm, Millipore Inc.). The dilute concentrations of 1, 5, and 10 mM were used to monitor the effects of the electrolyte using AFM.

2.2. PM-IRRAS Measurements at the Air/Electrolyte/Solid Interface. An iS50R Fourier transform infrared spectrometer (Thermo Scientific, Inc.) instrument with aluminum mirrors was used to collect PM-IRRAS infrared reflectance absorbance spectra and ATR−FTIR spectra of the samples. An in-house built (by the Perrine research group) optical set up was coupled to the same instrument to collect PM-IRRAS, as described previously.[13,35] The polished iron samples were attached to the sample holder in a vertical orientation, as shown in Figure 1A. A photoelastic modulator (PEM, Hinds, Inc.) with a ZnSe polarizer was placed in the beam path to modulate the signal between p and s polarized light. The half wave of the Bessel function was set to 2100 cm^{-1} to collect PM-IRRAS of iron interfaces of electrolytes dissolved in nanopure water. The half wave was changed to 1800 cm^{-1} to collect PM-IRRAS of iron interfaces of electrolytes dissolved in D_2O, so that the stretching and bending vibrational modes of water could be seen clearly on the Bessel function background. The PM-IRRAS spectrum of the sample within the 4000−600 cm^{-1} spectral region was recorded using 4.0 cm^{-1} resolution, a gain of 8.0, an aperture of 5%, and 1000 scans.

The optical alignment onto the iron surface and the optimization of the peak-to-peak (p/p) signal were carried out as described previously.[13,35] Several types of spectra were collected under the different stages of corrosion of iron with either 10 mM $CaCl_2$(aq) or 10 mM NaCl(aq) electrolytes. First, a spectrum of the dry, polished iron sample was collected before starting the corrosion reaction. Next, an empty beaker was placed under the polished iron sample and filled with nanopure water until the p/p signal was reduced by half, showing that the water attenuated the p/p signal. This ensured that the sample surface can still be detected through the solution. The water/iron interface spectra were recorded to check that no other features were observed at the air/water/Fe interface.

Next, the 100 mM NaCl(aq) or the 50 mM $CaCl_2$(aq) solution was diluted in the 50 mL beaker such that the final electrolyte concentration was 10 mM, as shown in Figure 1A. The volume in the beaker was suitably adjusted to keep the electrolyte/iron interface in the IR beam pathway by monitoring the p/p signal of the interferogram. Once this was achieved, the PM-IRRAS spectra were recorded over a total time of 1 h (denoted as stage 1). Next, 50 μL aliquots of the electrolyte solutions were removed, and PM-IRRAS spectra were collected after each removal of each aliquot (denoted as stage 2). This step allowed for atmospheric O_2 and CO_2 (air) to adsorb to the electrolyte/iron interface, initiating the corrosion reaction, which is notated as the air adsorption step. This process was continued until the p/p signal had returned close to its original value. Then, the electrolyte in the beaker was removed so that the iron sample was not in contact with the electrolyte. This allowed the iron interface to oxidize in air, notated as the air oxidation step (stage 3). The PM-IRRAS spectra were then collected, until no change in the reflectance modes was observed.

2.2.2. Fitting of PM-IRRAS Data. The Bessel function baseline was corrected by subtracting the PM-IRRAS spectra of the dry iron with an empty beaker in place from each spectrum during adsorption of atmospheric O_2 and CO_2 during carbonate formation (stage 2) and air oxidation (stage 3). Representative data from our experiments are shown below with the raw data shown in Figure S1 in the Supporting Information section. Peak areas of each surface species were analyzed by fitting the PM-IRRAS spectra to obtain the rate of oxidation and formation of each mineral at the interface. A linear baseline was fit to each region of the Bessel function where vibrational modes were present. The PM-IRRAS spectra were fitted using 100% Gaussian lineshape in CasaXPS software. The total peak areas for the δOH, νCO_3, and δFe−CO_3 vibrational modes were each summed to obtain the total area contribution of each mode for each PM-IRRAS spectrum in the air adsorption step and the air oxidation step.

2.3. ATR−FTIR Spectroscopy. The ATR−FTIR spectra were collected after the PM-IRRAS experiments at the interface region and the submerged region of the samples, as shown in the images in Figure 1A. The Fe samples used for PM-IRRAS experiments were directly used for ATR−FTIR analysis without rinsing with water. Spectra were collected on an external ATR attachment with a diamond ATR crystal using 256 scans per spectrum, a resolution of 4.0 cm^{-1}, and a gain of 4.0. A pressure pin was used to press the samples against the diamond ATR crystal. A spectrum of the clean, uncorroded iron was used as background for the corroded interface and submerged regions. The ATR−FTIR spectra of natural mineral specimens were also collected for comparison using the bare ATR cell as background. Mineral specimens were loaned from the A. E. Seaman Mineral Museum at Michigan Tech. Specimens of siderite (DM23948), aragonite (DM24902), calcite (personal collection), lepidocrocite (DM22910), and goethite (DM6809) were collected.

2.4. X-ray Photoelectron Spectroscopy. A PHI 5800 XPS instrument (PerkinElmer, Physical Electronics model) was used to analyze the elemental composition of surface species and their chemical states on different regions of the polished iron samples after exposure to $CaCl_2$(aq) and NaCl(aq) electrolytes. The base pressure of the XPS instrument was kept at ultrahigh vacuum (1×10^{-9} Torr) pressures. A Mg anode (1253.6 eV) at 15 kV voltage was used to analyze the surface of the iron samples used in the PM-IRRAS experiments before and after corrosion. The analysis diameter on the sample was 800 μm, and the angle between the sample and the analyzer was maintained at 45°, where the angle between the anode and the analyzer was 54.6°. Three different regions on the iron surface were analyzed: (1) the polished, uncorroded iron surface that did not come in contact with the electrolyte, (2) the interface region that was analyzed in the PM-IRRAS experiments, and (3) the region that was submerged in the electrolyte solutions (see images in Figure 1A). Survey spectra were collected using a pass energy of

https://doi.org/10.1021/acs.jpca.1c06451
J. Phys. Chem. A 2021, 125, 8047−8063

187.85 eV, a step size of 0.8 eV, and a dwell time of 20 ms/step.

High-resolution energy scanning was collected for the C 1s, O 1s, Na 1s, Fe 2p, Ca 2p, and Cl 2p regions using a pass energy of 23.50 eV, a step size of 0.1 eV, and a dwell time of 100 ms/step. XPS spectra of the natural mineral specimens are shown in Supporting Information. The mineral specimens were not sputtered as the sputtering was found to change the stoichiometry of the elemental composition. All XPS spectral peaks were fitted using CasaXPS software. A Shirley background was used for the baseline correction, and the peaks were deconvoluted using 100% Gaussian lineshapes. All the regions were charge-corrected with respect to the aliphatic carbon in the C 1s region at a binding energy of 284.6 eV.

2.5. Liquid AFM. The nanoscale topography of surface corrosion on the Fe surface was studied by *in situ* liquid AFM. Different concentrations of 1, 5, and 10 mM of NaCl(aq) or $CaCl_2$(aq) were applied to clean iron surfaces to monitor the effects of varying concentrations of the electrolyte. All AFM images were collected using the Asylum MFP-3D Origin AFM instrument in a horizontal orientation, as shown in the images in Figure 1B

Prior to corrosion, AFM images of the dry iron samples were collected. The Fe sample was mounted to a glass slide using carbon tape. The exposed parts of the glass slide were covered with parafilm to prevent spilling of the liquid off the sample stage. Aluminum-coated monolithic silicon tips (Tap300Al-G, Budget Sensors) with a 40 N/m force constant and 300 kHz resonant frequency were used to image the samples. The clean, dry Fe surface was imaged using the tapping mode (AC Air mode) of image sizes of 20 μm × 20 μm, 10 μm × 10 μm, and 5 μm × 5 μm, using an average scan rate of 1.0 Hz and 256 points per line. Slower scan rates (between 0.5 and 1.0 Hz) were used to collect images of the iron surfaces after corrosion.

AFM of Fe surfaces were imaged *in situ* while exposed to liquid solutions. Following the collection of the dry Fe surface, approximately 60 μL of either the NaCl(aq) or the $CaCl_2$(aq) electrolyte solution was added to the Fe surface, creating a bubble droplet on the Fe surface, as illustrated in Figure 1B. In liquid, a gold- and chromium-coated cantilever (BL-TR400PB, Asylum Research) was used in the tapping mode in the liquid (AC water mode). A couple of 20 μL droplets of the electrolyte were placed around the cantilever, to prevent the production of bubbles during engagement. The cantilever was immersed into the electrolyte solutions of 1, 5, or 10 mM at the same location at which the AFM images were collected on the dry Fe surface. AFM images of 10 μm × 10 μm and 5 μm × 5 μm areas were continuously collected at an average scan rate between 0.50-0.70 Hz and 256 points per line. The corrosion of the Fe surface was imaged over time ranges between 120 to 600 min. The electrolyte solutions were exposed to the Fe surface for several hours as time permitted during the experiment, which depended on how well the tip could image in solution without losing tracking of the tip with the laser: 4.7 h (1 μM $CaCl_2$(aq)), 7.5 h (5 mM NaCl(aq)), 4.5 h (5 mM $CaCl_2$(aq)), and 5 h (10 mM NaCl(aq)). Liquid AFM images were also collected on an uncorroded Fe surface using nanopure water, which served as a standard for comparison between the AFM images collected in the electrolyte solutions.

2.6. *Ex Situ* AFM: Air Oxidation of Iron. At the end of the experiment, the electrolyte solution was rinsed off the iron surface with nanopure water to remove excess particles not adsorbed to the surface. The sample was left to dry in air for 30 min prior to imaging. The corroded surface was imaged using tapping mode in air to identify the changes in surface topography after air oxidation. The baseline of all the images was flattened using a third-order correction. The surface roughness was analyzed by collecting the root mean square (RMS) values of the Fe surface before, during, and after corrosion using 1 μm × 1 μm sized boxes and averaging over five areas in each AFM image.

3. RESULTS

3.1. Interfacial O_2 and CO_2 Adsorption on the Iron Interface. The corrosion reaction of the polished iron interface in the $CaCl_2$(aq) and NaCl(aq) electrolytes was measured in three different stages: (1) PM-IRRAS of the iron surface in either 10 mM $CaCl_2$(aq) or the 10 mM NaCl(aq) at the air/electrolyte/iron interface, (2) adsorption of atmospheric O_2 and CO_2 (from air) by decreasing the volume of solution in 50 μL aliquots, and (3) oxidation in air (from atmospheric O_2 and CO_2) at the air/iron interface. First, the PM-IRRAS spectrum of the clean, dry iron surface was collected to confirm that foreign species were not present on the surface and it was free of contamination. The polished Fe surface has a native oxide layer present on the surface in ambient conditions, which is not visible in the PM-IRRAS spectrum. Iron samples were then vertically half submerged in nanopure water. Only two reflectance peaks were observed, from water stretching (νOH) between 3600 and 3200 cm^{-1}, and water bending (δOH) modes between 1650 and 1620 cm^{-1} which are attributed to liquid water, as observed in our previous results.[13] No new reflectance peaks were observed other than water νOH and δOH modes within 1 h. These are further supported by experiments in D_2O, where the νOD and δOD modes are only present when the solution is on the iron surface (see Figure S2 in Supporting Information). Next, the iron sample was submerged in either 10 mM $CaCl_2$(aq) or 10 mM NaCl(aq), and PM-IRRAS spectra were continuously collected until no further changes were observed in the PM-IRRAS spectra (approximately 1−2 h) at the air/electrolyte/iron interface, as shown in Figure 1, where zero minutes represent when the sample was first submerged in the electrolyte.

In stage 2, 50 μL aliquots of the electrolyte solution ($CaCl_2$(aq) or NaCl(aq)) were removed before collecting each PM-IRRAS spectrum, shown in Figure 2. This allowed for adsorption of atmospheric O_2 and CO_2 (from air) to the electrolyte/iron interface and initiating the corrosion process. Three distinct reflectance peaks were observed as CO_2 and O_2 react with the iron surface, as given in Figure 2: δOH modes, νOH modes within the 3600−3200 cm^{-1} region (see Figure S1 in Supporting Information), and νCO_3 stretching modes from adsorbed carbonate species. The δOH modes were observed between the 1622 and 1633 cm^{-1} region for Fe in $CaCl_2$(aq) compared to those observed between 1622 and 1665 cm^{-1} for Fe in NaCl(aq). With increasing O_2 and CO_2 adsorption and over time, the δOH modes remain constant within the 1622−1635 cm^{-1} region for Fe in $CaCl_2$(aq) but blue shifts from 1622 to 1665 cm^{-1} for Fe in NaCl(aq). The presence of the δOH mode and the νCO_3 stretching modes for Fe exposed to $CaCl_2$(aq) is attributed to growth of bicarbonate species on the surface from adsorbed hydroxylated species.[36−38] In comparison to Fe in NaCl(aq), the δOH mode

https://doi.org/10.1021/acs.jpca.1c06451
J. Phys. Chem. A 2021, 125, 8047−8063

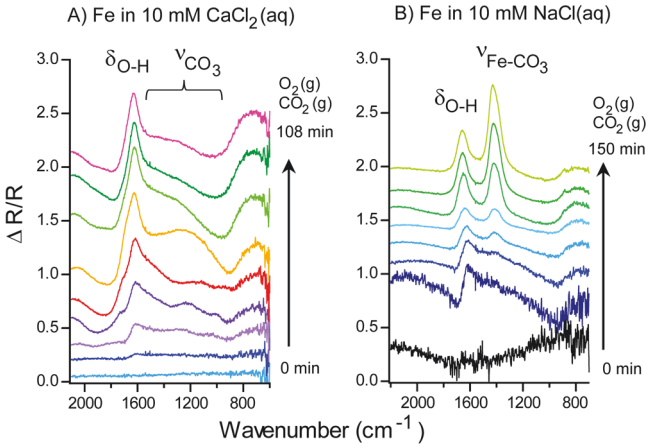

Figure 2. PM-IRRAS spectra of iron in 10 mM (A) $CaCl_2$(aq) or (B) NaCl(aq) solution with adsorption of O_2 and CO_2 from air. Reflectance spectra show the formation of CO_3 and hydroxyl modes at both types of interfaces over time (in minutes). O_2 and CO_2 in air were adsorbed to the air/electrolyte/Fe interface by removing 50 μL aliquots, and PM-IRRAS spectra were measured over several minutes. Plot B is reproduced in part with permission from [de Alwis, C.; Perrine, K. A., In situ PM-IRRAS at the air/electrolyte/solid interface reveals oxidation of iron to distinct minerals. *J. Phys. Chem. A* **2020,** *124* (33), 6735−6744] Copyright 2020 American Chemical Society.

disappeared after the solution was removed and is attributed to the presence of liquid water[13] at the air/liquid interface.

It is evident in Figure 2A,B that the intensity of the δOH mode gradually increases over time in both experiments. The data suggest that as the aliquots of electrolytes ($CaCl_2$(aq) or NaCl(aq)) are removed, atmospheric O_2 or CO_2 from air adsorbs to the interface region, resulting in hydroxylated species on the surface from surface oxidation or from dissolved species in the electrolyte. It is unclear if atmospheric CO_2 adsorbs directly or quickly dissolves into solution creating carbonic acid, HCO_3^-, or CO_3^{2-}. Our previous results do not show substantial growth of carbonates in nanopure water over the same time period, so we attribute our results to dissolved ions at the interface or direct adsorption of atmospheric CO_2. In the case of NaCl(aq), the δOH disappears, after the solution is completely removed, showing that the peak is assigned to liquid water. For iron in $CaCl_2$(aq), the δOH mode continues to grow as O_2 and CO_2 adsorb to the interface region in Figure 2A. During the adsorption process, the surface of the iron becomes rough, affecting the reflection of the IR beam and distorting the Bessel function shape in both experiments (shown in Figures S2 in Supporting Information). This distortion of the Bessel function of iron in $CaCl_2$(aq) is more severe compared to iron in NaCl(aq) and could be due to the growth of an insoluble film, attenuating the reflected light to the detector. Apart from the hydroxyl surface species, broad νCO_3 modes are shown between 1470 and 1502 cm^{-1} for Fe in $CaCl_2$(aq) from bidentate binding and sharp νCO_3 modes are shown between 1415 and 1430 cm^{-1} for Fe in NaCl(aq), suggesting a monodentate binding.[13]

The peak areas for the δOH (or δOD) and νCO_3 modes were fitted from the spectra in Figure 2 and other experiments (see Supporting Information) with Gaussian curves. The peak areas were normalized to the maximum peak area of the air-oxidized areas in Figure 3, defined as the relative coverage, θ. This allowed for tracking the rate of formation of the carbonate mineral growth at the iron interface. The coverage of the peak

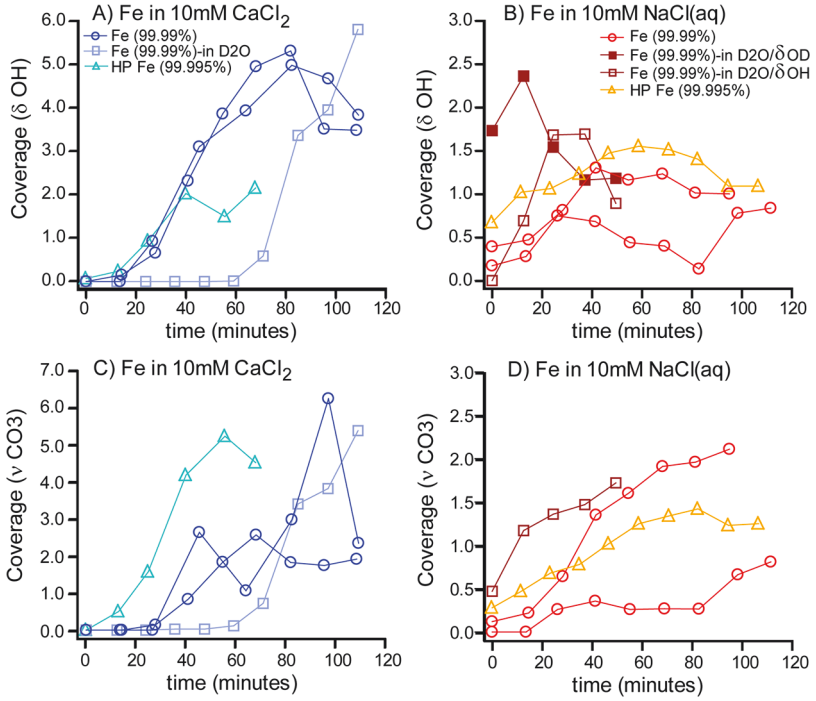

Figure 3. Peak area analysis for the surface coverage of the δOH or the δOD mode for Fe in (A) 10 mM $CaCl_2$(aq) and (B) 10 mM NaCl(aq) and the coverage of the νCO_3 mode for Fe in (C) 10 mM $CaCl_2$(aq) and (D) 10 mM NaCl(aq). The coverage was computed using the total peak area for each mode divided by the maximum peak area during air oxidation. Color scheme: (blue circles) Fe (99.99%) in $CaCl_2$(aq), (light blue triangles) Fe (HP, 99.995%) in $CaCl_2$(aq), (blue squares) Fe (99.99%) in D_2O−$CaCl_2$(aq), (red circles) Fe (99.99%) in NaCl(aq), (yellow triangles) Fe(HP, 99.995%) in NaCl(aq), and (maroon squares) Fe (99.99%) in D_2O−NaCl(aq).

https://doi.org/10.1021/acs.jpca.1c06451
J. Phys. Chem. A 2021, 125, 8047−8063

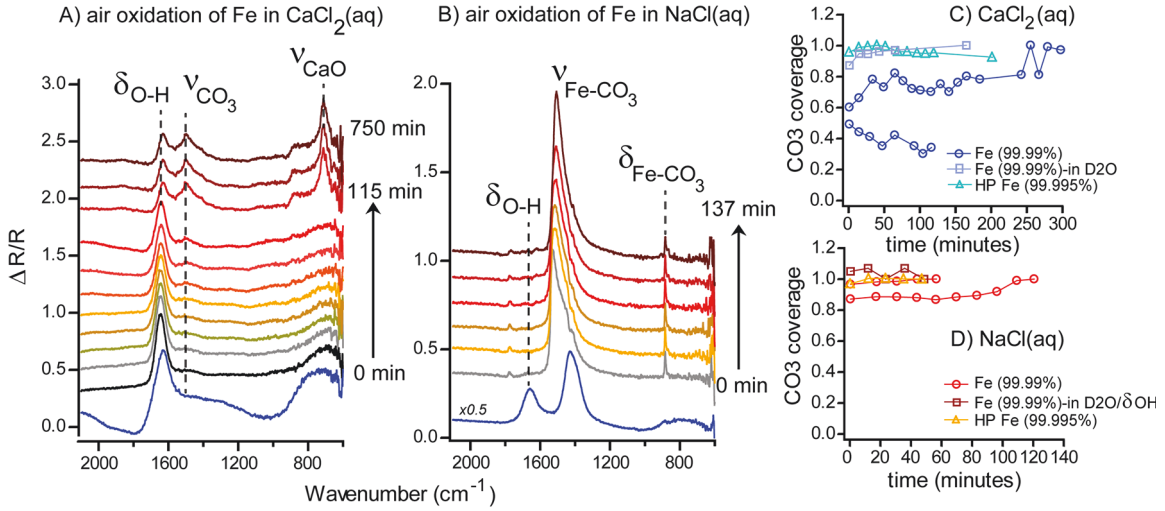

Figure 4. Air oxidation of iron exposed to (A) $CaCl_2$(aq) and (B) NaCl(aq). The blue spectrum is the last spectrum in solution before completely removing all the solution for air oxidation. Peak area plots shown to the right of the spectra show little change over time after air exposure, (C) carbonate coverage for iron in $CaCl_2$(aq), and (D) carbonate coverage for iron in NaCl(aq). The marker color scheme is the same as in Figure 3. Plot B is reproduced in part with permission from [de Alwis, C.; Perrine, K. A., In situ PM-IRRAS at the air/electrolyte/solid interface reveals oxidation of iron to distinct minerals. *J. Phys. Chem. A* **2020**, *124* (33), 6735−6744] Copyright 2020 American Chemical Society.

areas is plotted as a function of time and shown for the δOH or δOD modes in Figure 3A,B and νCO_3 modes in Figure 3C,D during air (O_2 and CO_2) adsorption, where time 0 is the first 50 μL aliquot of the electrolyte removed. Figure 3 illustrates the variation of atmospheric O_2 and CO_2 adsorption on four different types of experiments: (1) two experiments for Fe (99.99%) exposed to each electrolyte, (2) Fe exposed to each electrolyte dissolved in D_2O, and (3) high-purity Fe (HP Fe, 99.995%) exposed to each electrolyte solution. For all types of experiments, the variation of both areas (δOH, δOD, or νCO_3) during O_2 and CO_2 adsorption to produce surface carbonates in both $CaCl_2$(aq) and NaCl(aq) increased over time. It should be noted that as these experiments were performed in air, a constant concentration of 760 Torr of air consisting of 20% O_2 and 0.04% CO_2 is being adsorbed over a finite area (analysis area of the PM-IRRAS signal). Therefore, the flux of atmospheric O_2 and CO_2 gas being adsorbed is constant to the surface and is plotted over time.

The area under the δOH or δOD mode on both iron samples (iron and HP iron and for experiments for electrolytes in D_2O) increases quickly for iron in $CaCl_2$(aq) in Figure 3A but increases gradually for Fe in NaCl(aq) in Figure 3B. The onset of corrosion for Fe in NaCl(aq) began prior to removing the solution at zero minutes. This can be observed in our previous study that prior to removing solution and adsorbing O_2 and CO_2, the δOH and νCO_3 modes appear.[13] For Fe in NaCl(aq), when O_2 and CO_2 are adsorbed, the area of the δOH mode initially increases (as the surface hydroxylation produces more hydroxyl groups on the Fe surface) and then decreases, due to the thinning of the liquid layer as the solution was removed gradually. For Fe in $CaCl_2$(aq), the curve for the δOH coverage plateaus after 60−80 min. These hydroxyl groups are basic and react directly with atmospheric CO_2(g) to form surface carbonates at the interface region. It should be noted that the electrolyte solutions were not sparged of dissolved O_2 or other gases. It is possible that atmospheric O_2 and CO_2 are adsorbing into the electrolyte thin film at the interface and reacting with the surface to produce surface carbonates. In previous benchmark experiments (see Supporting Information)[13] in nanopure water with no ions, no surface carbonates or oxides were observed in the same time frame of the PM-IRRAS experiments. Our measurements show clear indication of surface oxidation to carbonates.

Figure 3C,D shows the change in the νCO_3 peak area coverage as a function of time for iron surfaces in $CaCl_2$(aq) and NaCl(aq), respectively. Similar to the plots in Figure 3A,B, the coverage of the νCO_3 mode quickly increases for Fe in $CaCl_2$(aq) compared to the gradual growth of carbonate (CO_3) for Fe in NaCl(aq). In the presence of $CaCl_2$(aq), the CO_3 layer forms quickly on the Fe interface, in Figure 3C, as compared to the rate of formation of $FeCO_3$ in Figure 3D. This suggests that once the CO_3 film is grown, the interface is saturated with CO_3, resulting in a plateau in Figure 3C. This difference in rate in Figure 3C and spectroscopic signatures in Figure 2A may be due to the formation of a different type of carbonate, such as $CaCO_3$(s) at the interface, compared to the gradual and steady increase in νCO_3 coverage in Figure 3D for $FeCO_3$ (siderite). Further evidence is shown visually in the video recording (see Supporting Information) on high purity (HP) iron, where HP Fe exposed to $CaCl_2$(aq) corrodes quicker and comes to a saturation point, but in NaCl(aq), the corrosion and mineral growth on the Fe surface continue gradually in air.

The overall analysis of the δOH and νCO_3 modes suggests that carbonate films are grown at a faster rate on the HP iron (HP Fe, 99.995%) exposed to $CaCl_2$(aq) and air (O_2 and CO_2) compared to the iron (99.99%) sample. This difference can be attributed to the increased concentration of trace anticorrosion metals (Cr, Ti, or Mo) present in the iron (99.99%), which slows the oxidation of the surface. The δOH coverage from Fe in $CaCl_2$(aq) also continues to grow, owing to a hydroxylated carbonate/bicarbonate film at the interface, suggesting that this δOH could also be from bicarbonate OH groups and not liquid water, as was shown for Fe in NaCl(aq).[13]

3.2. Air Oxidation of Iron. After the electrolytes were completely removed from the iron interface, the surface was allowed to oxidize in air from exposure to atmospheric O_2 and

https://doi.org/10.1021/acs.jpca.1c06451
J. Phys. Chem. A 2021, 125, 8047−8063

CO_2. The PM-IRRAS spectra were collected continuously until no further spectral changes were observed, as shown in Figure 4A,B, where time zero is the first spectrum collected after all the electrolyte was removed. The PM-IRRAS spectra collected at the air/electrolyte/Fe interface for iron exposed to 10 mM $CaCl_2$(aq) show three peaks in Figure 4A. The peak at 1646 cm^{-1} is assigned to δOH modes of hydroxylated species from either HCO_3^- on the iron surface (or partially due to remaining adsorbed water on the Fe surface). The other two peaks are observed at 1504 and 885 cm^{-1}, assigned to the asymmetric νCO_3 mode and the δCO_3 deformation mode, respectively.[39,40] The broad νCO_3 mode that appears at 1420 cm^{-1} is blue shifted to 1504 cm^{-1} as the Fe surface oxidizes in air, likely due to the restructuring of bonding modes (monodentate, bidentate, and bridged) of carbonate on the Fe surface. In parallel, the intensity of the δOH mode at 1630 cm^{-1} decreases as the adsorbed water layer evaporates during air oxidation but does not completely disappear as was shown for Fe in NaCl(aq).[13] Another mode is observed at 712 cm^{-1} that is assigned to the νCa−O mode, suggesting that Ca is grown into the oxide on the surface.[39,40] This observation indicates that bicarbonates are present after adsorption of atmospheric CO_2 on the hydroxylated Fe surface to form $CaCO_3$ or $FeCO_3$. The PM-IRRAS spectra of Fe exposed to 10 mM NaCl(aq) is shown for comparison in Figure 4B. The two major peaks that appear between 1530 and 1510 cm^{-1} and at 886 cm^{-1} were previously assigned to the νCO_3 mode and the deformation mode of $FeCO_3$, respectively. The presence of the νCO_3 and νCa−O modes indicates that both $CaCO_3$(s) and $FeCO_3$(s) are both grown on the surface at the air/electrolyte/Fe interface.

The corrosion process is dynamic during air oxidation, leading to a restructuring process of the $FeCO_3$ into monodentate carbonates from CO_2 adsorption. Figure 4C,D shows the variation of CO_3 coverage on Fe exposed to $CaCl_2$(aq) and NaCl(aq) during air oxidation. Figure 4C illustrates the variation of CO_3 adsorption on four Fe samples exposed to $CaCl_2$(aq) under three different surface conditions: (1) two Fe (99.99%) samples exposed to $CaCl_2$(aq), (2) Fe exposed to $CaCl_2$ dissolved in D_2O, and (3) HP (99.995%) Fe exposed to 10 mM $CaCl_2$(aq). All data show that the CO_3 surface coverage increases slightly over time from additional oxidation, but the rate of CO_2 adsorption has flatlined. Similar results are observed for the CO_3 coverage on Fe exposed to NaCl(aq) in Figure 4D: (1) two Fe (99.99%) samples exposed to NaCl(aq), (2) Fe exposed to NaCl dissolved in D_2O, and (3) high purity (HP, 99.995%) Fe exposed to 10 mM NaCl(aq). The rate of formation of CO_3 over time is small within the time period of the experiment as the surface may be saturated with CO_3 species and no more reaction sites are available for additional atmospheric CO_2 or CO_3^{2-} adsorption. It is also possible that multilayer carbonate films grown on the surface have a significantly slower growth rate in air compared to ionic carbonate species in the electrolyte solution.

3.3. *Ex Situ* Analysis of Post Air Oxidation. After PM-IRRAS, *ex situ* analysis of the iron samples was conducted using ATR−FTIR spectroscopy and XPS to analyze the differences of surface species and elemental composition between the interface region and the region submerged in electrolyte solutions (see Figure 1A). There were three visually distinguishable regions on iron surfaces used for the PM-IRRAS experiments: the interfacial region (air/electrolyte/Fe), the submerged area in electrolyte ($CaCl_2$(aq) or NaCl(aq)) solution, and the polished (noncorroded) area that was kept above the electrolyte level during the PM-IRRAS corrosion experiments.

The ATR−FTIR spectra in Figure 5 of the interface in spectra 5A and 5C and in the submerged region in spectra 5B

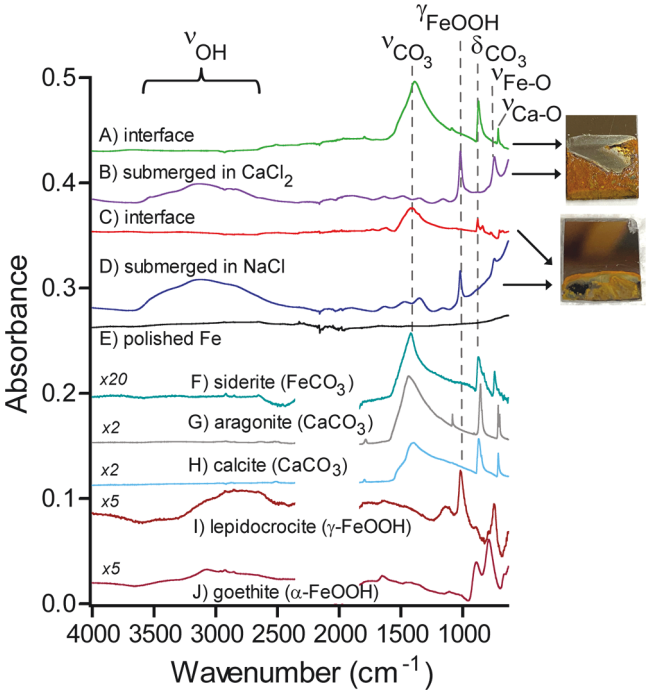

Figure 5. ATR−FTIR spectra of the interface vs submerged region spectra for corroded iron surfaces, compared to natural mineral specimens for identification of vibrational modes. (A) Interface region of iron exposed to $CaCl_2$(aq), (B) submerged region of iron exposed to $CaCl_2$(aq), (C) interface region of iron/NaCl(aq), (D) submerged region of iron/NaCl(aq), (E) polished iron, (F) siderite, (G) aragonite, (H) calcite, (I) lepidocrocite, and (J) goethite. Arrows point to the region collected on samples in photographs. Spectral intensities are multiplied for qualitative comparison with corrosion products on the iron surfaces.

and 5D are shown for both Fe samples exposed to $CaCl_2$(aq) or NaCl(aq) compared to natural mineral specimens (5F−J) and the polished Fe surface prior to corrosion (5E). The interface regions for iron exposed to either electrolyte show clear evidence of growth of carbonate mineral films from the exposure of atmospheric CO_2 to the air/electrolyte/Fe interface. These spectra are compared with ATR−FTIR spectra of carbonate minerals, (5F) siderite ($FeCO_3$), (5G) aragonite ($CaCO_3$), (5H) calcite ($CaCO_3$), and with iron oxyhydroxide minerals, (5I) lepidocrocite (γ-FeOOH), and (5J) goethite (α-FeOOH). The polished Fe surface (5E) has only the presence of a native oxide and hydroxide species, which have smaller features compared to the visible spectra from the corrosion products in spectra 5A−D.

At the interface, signature νCO_3 modes at 1393 cm^{-1} for $CaCO_3$ on iron in $CaCl_2$(aq) in spectrum 5A and at 1409 cm^{-1} in NaCl(aq) in spectrum 5C are similar to the vibrational signatures for the minerals in spectrum 5F siderite (1419 cm^{-1}), spectrum 5G aragonite (1440 cm^{-1}), and spectrum 5H calcite (1399 cm^{-1}). Other key vibrational signatures of $CaCO_3$ are observed in spectrum 5A at the interface region at 1090, 871, and 711 cm^{-1}, in agreement with the natural

https://doi.org/10.1021/acs.jpca.1c06451
J. Phys. Chem. A 2021, 125, 8047−8063

Table 1. ATR−FTIR Spectroscopic Vibrational Modes and Assignments

sample	region	νOH	νC═O	δOH	νCO_3	γ-FeOOH		δ-FeOOH	δCO_3	νFeO	νCaO
Fe(HP)/$CaCl_2$(aq)	interface		1796		1393		1090		871		711
	submerged	3138		1638	1484, 1351	1160	1019	892		742	
Fe(HP)/NaCl(aq)	interface	3280		1620	1409				877, 837		
	submerged	3113		1633	1470, 1350	1160	1021			744	
aragonite	mineral		1788		1440		1082		854		711, 700
calcite	mineral		1798		1399				871		711
siderite	mineral				1419				875	742	
lepidocrocite	mineral	2840				1139	1018	893		746	
goethite	mineral	3075		1653	1441		1113	889		789	

mineral spectral features of aragonite and calcite.[39,40] On the Fe surface exposed to NaCl(aq) in spectrum 5C, $FeCO_3$ is formed as a corrosion product (5F), as shown from the observed νCO_3 and δCO_3 modes at 1409 and 877 cm^{-1}, respectively.[38,41] The carbonate film formed on the Fe interface in the presence of $CaCl_2$(aq) (spectrum 5A) can be assigned to the growth of $CaCO_3$, a visible white film that was observed at the interface. The additional observation of νCa−O modes at 711 cm^{-1} agrees with the assignment.[40,42] We can identify that Fe exposed to $CaCl_2$(aq) produces either aragonite, calcite, or a combination of the two at the air/electrolyte/Fe interface and iron exposed to NaCl(aq) produces siderite ($FeCO_3$).

In the submerged region of the Fe surface that was not detected by PM-IRRAS in Figure 5B,D, a combination of carbonate and hydroxide vibrational modes is observed, suggesting the growth of lepidocrocite and a different form of iron hydroxide carbonate. These modes and assignments are listed in Table 1. Strong evidence for distinct carbonates[38,43] is observed at 1350 and 1470 cm^{-1} in spectrum 5B for Fe exposed to $CaCl_2$(aq) and in spectrum 5D for $FeCO_3$ for iron exposed to NaCl(aq). In the submerged region in both electrolytes, similar vibrational signatures are also observed that resemble the signature of lepidocrocite (spectrum 5I). These modes at 1018 cm^{-1} and 746 cm^{-1} are from the γ-FeOOH mode and the νFeO mode, respectively, along with νOH modes suggesting that lepidocrocite is produced.

3.3.1. XPS Analysis. The interface, submerged, and polished Fe regions of both types of samples were analyzed using XPS of the C 1s, O 1s, and Cl 2p regions, shown in Figure 6A−E. The uncorroded, polished iron surface prior to exposure to the electrolyte solutions is covered with a thin native oxide/hydroxide layer. These peaks are identified in the O 1s region in Figure 6E: iron oxide (Fe−O), Fe hydroxide (Fe−OH), and adsorbed water (H_2O). After Fe is exposed to the electrolyte solutions of $CaCl_2$(aq) or NaCl(aq), new features appear at binding energies of 529.0−529.6 eV, attributed to iron oxide (Fe−O), in agreement with binding energies collected for lepidocrocite and goethite mineral samples[44] (see Figure S5 in Supporting Information). Adsorbed surface carbonate (CO_3) is observed at higher binding energies near 531.5−531.9 eV assigned to $CaCO_3$ and at 530.8 eV for $FeCO_3$, similar to those for calcite and siderite (see Figure S5).[45,46] It is difficult to distinguish surface carbonate from hydroxylated species (Fe−OH), as both O 1s binding energies from Fe−OH and CO_3 overlap within 531.0−532.0 eV.[47,48] Therefore, we have assigned just one peak in the O 1s region for representing both OH and CO_3 species.

Evidence of surface carbonate is also observed on all Fe surfaces exposed to either electrolyte in the C 1s region at 290.1 eV or bicarbonate at 290.8 eV, respectively. These surface species were also observed for calcite, siderite, and aragonite minerals at 288.6−291.0 eV (see Figure S6 in Supporting Information) and in agreement with the aforementioned PM-IRRAS and ATR−FTIR analysis. The binding energy in the C 1s region for (6C,D) Fe exposed to NaCl(aq) was found at 289.3 eV for $FeCO_3$ and at 290.3 eV for $CaCO_3$ (6A,B) for Fe exposed to $CaCl_2$(aq). On a clean Fe surface, no carbonate was detected in the C 1s region, in Figure 6E. Other common features in the C 1s region were adventitious carbon at 284.6 eV, alcoholic (C−O) species at 286.0 eV, and carbonyl (C═O) species at 288.1 eV, as shown in Figure 6.[45,46,49,50]

The spectra in the Cl 2p region of Fe surfaces exposed to the electrolytes are shown in the last panel in Figure 6, where two types of chlorides were detected on both the interfacial region and the submerged region of the iron surface. The primary species for the Cl $2p^{3/2}$ peak is located at a binding energy of 198.5 eV is assigned to Ca−Cl species for iron exposed to 10 mM $CaCl_2$(aq) in Figure 6A,B.[45,46] The second Cl $2p^{3/2}$ peak is located at 200.1 eV is assigned to an Fe−Cl species, as chloride has high affinity to iron metal producing either $FeCl_2$ or $FeCl_3$.[44] In the Cl 2p region, two peaks were also observed for Fe exposed to 10 mM NaCl(aq) in Figure 6C,D, at 198.1 eV in agreement with the binding energy of Cl−Na in NaCl(aq)[51] and at 199.5 eV, which is due to a Cl−Fe species. Because iron has a higher oxidation state (Fe^{2+} or Fe^{3+}) compared to Na^+, the Cl $2p^{3/2}$ values of Fe−Cl should be shifted toward higher binding energies compared to Na−Cl or Ca−Cl as observed in XPS data. Signals from the Cl^-, Ca^{2+}, and Na^+ ions were detected as surface species as these samples were not rinsed after PM-IRRAS experiments before collecting XPS spectra.

The polished iron (noncorroded area) surface should not contain any chloride as it did not have any direct contact with the electrolytes. A small amount of chloride was observed, from residual exposure leftover from the polishing procedure or salt residue (Figure 6E). Significant concentrations of chloride are observed at the interface region exposed to $CaCl_2$(aq), compared to any other region, due to twice as much chloride present in the electrolyte compared to NaCl(aq). The binding energies were also analyzed for the Na 1s, Ca 2p, Fe 2p regions and compared to the XPS spectra of the natural mineral specimens. The areas of Ca 2p and Na 1s regions were analyzed (shown in Figure S7−S9 in the Supporting Information section) and confirmed the presence of residual NaCl in the Na 1s region at 1071.0−1071.9 eV and $CaCl_2$ or $CaCO_3$ at 347.4−347.6 eV. The $CaCl_2$ and $CaCO_3$ have very close Ca $2p^{3/2}$ binding energies within the 347.6−347.9 eV region, which make it difficult to precisely distinguish

https://doi.org/10.1021/acs.jpca.1c06451
J. Phys. Chem. A 2021, 125, 8047−8063

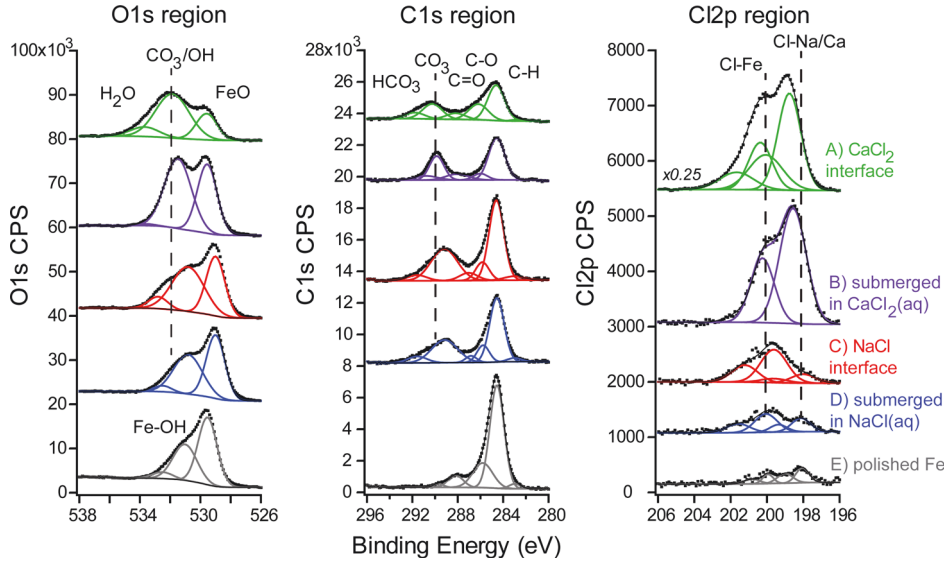

Figure 6. High resolution XPS regions of the O 1s, C 1s, and Cl 2p regions from the samples after PM-IRRAS experiments. (A) Interface region of Fe exposed to $CaCl_2$(aq) (green), (B) submerged region of Fe exposed to $CaCl_2$(aq) (purple), (C) interface region of Fe exposed to NaCl(aq) (blue), (D) the submerged region of Fe exposed to NaCl(aq) (red), and (E) polished iron surface (gray). Results indicate a large concentration of CO_3 species on the samples exposed to $CaCl_2$(aq) and NaCl(aq), relative to the C−H peak and the Fe−O at interface and submerged regions. Larger concentrations of Cl species are also observed at interface and submerged regions.

Table 2. XPS Ratios Quantifying the O/Fe, C 1s CO_3/Fe, and Cl/Fe Ratios and O 1s CO_3/Fe

		elemental peak area ratios						
sample	region	CO_3(C 1s)/ Fe 2p	CO_3(C 1s)/ Ca 2p	CO_3 (O 1s)/ Fe−O (O 1s)	Cl 2p/ Fe 2p	Ca 2p/ Fe 2p	Na 1s/ Fe 2p	total O 1s/ Fe 2p
$CaCl_2$/Fe	interface	1.78	0.43	3.38	3.99	4.14		10.73
	submerged	0.48	0.50	1.38	0.38	0.96		5.10
NaCl/Fe	interface	1.23		1.19	0.08		1.74	4.90
	submerged	0.86		0.86	0.09		1.54	4.06
polished Fe	n/a	0.04	0.34	0.66	0.05	0.11		3.44
aragonite			0.60					
calcite			1.03					
siderite		0.81		2.41				5.06
goethite								4.07
lepidocrocite			1.06					16.92

between these surface species.[45,46] The binding energy of $CaCl_2$ is reported at 348.0 eV and $CaCO_3$ is reported at 346.6 eV.[52] The binding energy for $CaCO_3$ falls within the 346.5−347.9 eV region,[50] which differs from the polymorphic type of $CaCO_3$ such as calcite and aragonite, shown in Figures S7B and S9B.[50,53] The Na 1s and Ca 2p regions show the presence of leftover NaCl and $CaCl_2$ at both the interface and the submerged regions. The Fe 2p region in Figure S8 shows the presence of iron oxide (Fe^{2+}/Fe^{3+}) and metallic Fe^0 prior to corrosion. After exposure to NaCl(aq), only a reduction in signal was observed. When Fe was exposed to $CaCl_2$(aq), the Fe^0 site at 706 eV disappears, owing to the transformation to oxidized Fe and growth of $CaCO_3$ on the surface. These spectra are compared to the Fe-containing mineral specimens, goethite, lepidocrocite, and siderite XPS spectra in the Fe 2p region in Figure S9A.

The relative peak areas of the XPS spectra for the C 1s, O 1s, Ca 2p, and Fe 2p regions were analyzed and are shown in Table 2 in comparison to the XPS ratios from the mineral specimens. The peaks areas from the high resolution spectra were normalized to the area of the entire Fe 2p region. Also, the peak areas that are assigned to the carbonate (CO_3) surface species are normalized to either the Ca 2p total area or the Fe−O peak area in the O 1s region to compare the relative concentrations of carbonate on the surface after the PM-IRRAS experiments. The relative concentration of ions from Cl^-, Ca^{2+}, and Na^+ were also assessed to determine the differences of ions at the interface regions compared to the submerged region.

The ratios of carbonate to iron (CO_3/Fe) and carbonate to calcium (CO_3/Ca) show that the interface region of Fe exposed to both electrolytes have more carbonates compared to the submerged region from adsorption of atmospheric CO_2. The CO_3/Fe or CO_3/Ca ratio should be 1:1 if $FeCO_3$ (siderite) or $CaCO_3$ (calcite or aragonite) is formed at the interface. However, differences in this ratio arise from the sensitivity factor correction for each XPS region or from the growth of a thin film. The CO_3 peak in the O 1s region at 531.5−531.9 eV includes both signals from surface CO_3 and from surface OH species. This species was normalized to the Fe−O (oxide) species at 529.0−529.6 eV, which indicates a relatively large concentration at the interface region compared to the submerged region. Iron oxides (total O 1s/Fe 2p ratio) are present at both the interface and the submerged regions of

https://doi.org/10.1021/acs.jpca.1c06451
J. Phys. Chem. A 2021, 125, 8047−8063

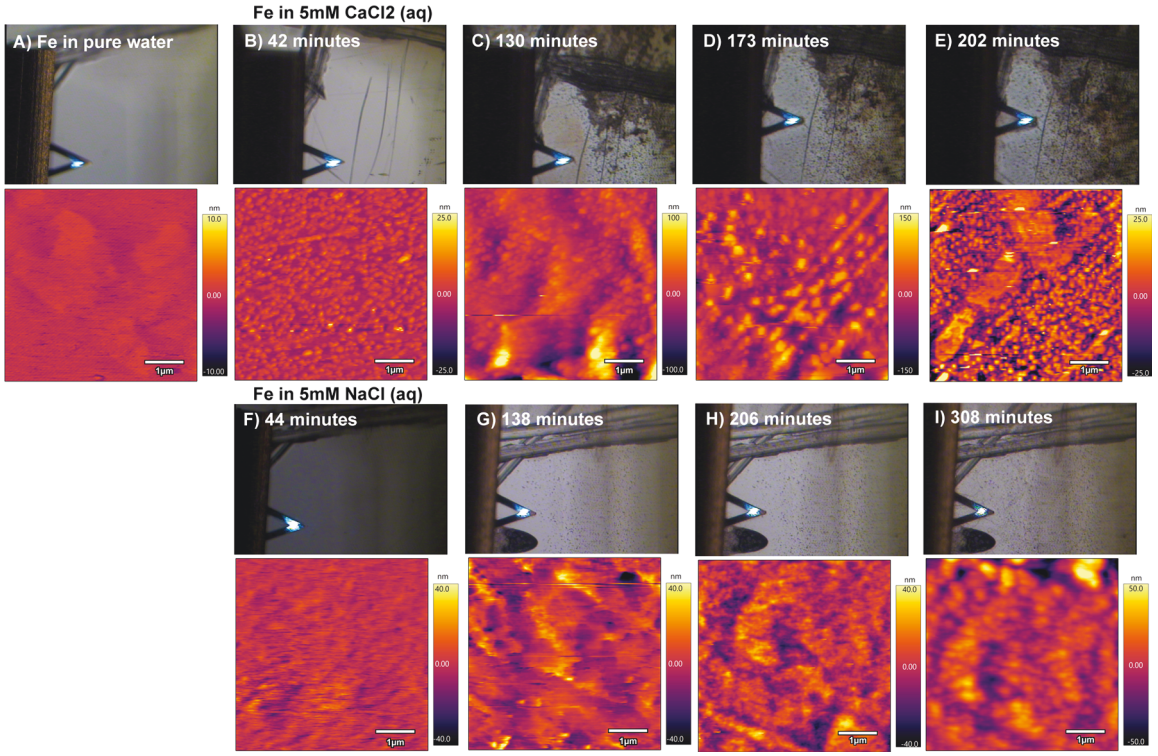

Figure 7. Iron surfaces in (A) nanopure water, (B–E) 5 mM $CaCl_2$(aq), and (F–I) 5 mM NaCl(aq). Representative images and photographs are shown as a function of time (minutes) in solution.

the samples, suggesting that additional oxidation of iron occurs after corrosion. A larger amount (4×) of Ca (Ca 2p/Fe 2p) and Cl (Cl 2p/Fe 2p) was observed at the interface region compared to the submerged region, whereas for Na (Na 1s/Fe 2p), the same relative amount was observed at the interface compared to the submerged region. This suggests that Ca^{2+} ions have a preference for the air/electrolyte interface and could play a role in the formation of $CaCO_3$.

A separate experiment was carried out to assess the presence of the ions and carbonate species after rinsing with nanopure water (not shown). A large amount of surface carbonates (from the C 1s region) was observed after rinsing and oxidizing in air for both Fe samples exposed to the electrolyte solutions. The Na was rinsed off in the process, but Ca and Cl remained on the surface, suggesting that the surface carbonates are grown onto the Fe surface. In summary, carbonates and chlorides are present on the iron surface after corrosion in the $CaCl_2$(aq) and NaCl(aq) electrolytes, in agreement with the PM-IRRAS and ATR–FTIR spectra shown in Figures 4 and 5.

3.4. AFM of Surface Corrosion. In order to further investigate the early stages of surface corrosion, the Fe surface was exposed to each diluted electrolyte solution and the surface topography was measured using *in situ* liquid AFM, as a function of time (in minutes). Figure 7 shows representative AFM images and camera images of Fe exposed to 5 mM $CaCl_2$(aq) and 5 mM NaCl(aq). It should be noted that AFM imaging in solution is quite challenging with loose particles in the droplet on the surface, as particles were found to float in solution and attract to the cantilever, thus affecting the tracking of the tip with the laser. The corrosion was too fast to observe in 10 mM concentrations with AFM; therefore, diluted solutions were used during the *in situ* liquid AFM measurements. Solutions of 1, 5, and 10 mM electrolyte concentrations were tested on new Fe surfaces, for every experiment. Only data are presented where sets of images for both $CaCl_2$(aq) and NaCl(aq) at the same concentration were successfully obtained.

Figure 7A shows the Fe surface in nanopure water, which did not exhibit any surface corrosion. Upon exposing the Fe surface to 5 mM $CaCl_2$(aq), as shown in Figure 7B–E, the particles appeared to grow from 10 nm in height (7B) into larger particles: 156 nm (7C), 317 nm (7D), and 164 nm (7E) in height. The surface was exposed to the solution for a total time of 275 min. This is in contrast to the Fe surface in 5 mM NaCl(aq), shown in Figure 7F–I, and small particles of 30 nm in height are initially observed in Figure 7F, followed by an increase in height over time: 51 nm (7G), 49 nm (7H), and 68 nm (7I). The total time the Fe surface was in solution was for 459 min. For both exposures, it can be seen from the optical images that the surface corroded over time, where the largest particle growth on the Fe surface was from exposure to $CaCl_2$(aq).

The surface roughness (RMS values) was evaluated to estimate the physical changes of the surface for iron in each solution from the AFM images, as shown from the plot in Figure 8. The average RMS was evaluated on all collected images using a 1 μm × 1 μm box size to average over several spots and plotted as a function of time (open markers). The start time (zero minutes) is the time the droplet of electrolyte solution was placed on the clean Fe surface. The RMS is an estimate of the corrosion rate, where pitting of the surface, dissolution of the Fe^{2+}, and deposition of particles in solution contribute to the physical changes of the surface. From Figure 8, we observe that the Fe surface exposed to $CaCl_2$(aq) had 3× faster rate of change of the surface roughness compared to Fe in NaCl(aq), by evaluation of the slope from linear regression (not shown). This may be due to the fact that more Cl^- ions and total charge are present in $CaCl_2$(aq) compared to the

https://doi.org/10.1021/acs.jpca.1c06451
J. Phys. Chem. A 2021, 125, 8047–8063

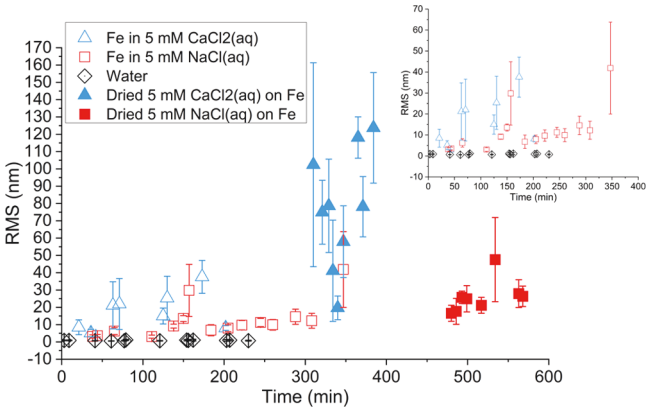

Figure 8. Plot of RMS of AFM collected on Fe in $CaCl_2$(aq), NaCl(aq), or nanopure water. These values are compared to the dried Fe surface after exposure to $CaCl_2$(aq),NaCl(aq) or nanopure water. The RMS plot shows that the rate of corrosion for the Fe surface in 5 mM $CaCl_2$(aq) (blue triangles) is faster compared to the Fe surface in 5 mM NaCl(aq) (red squares) and the Fe surface in water (black diamonds). The inset shows a zoomed-in plot of the RMS values from the Fe surface in the electrolytes. The filled-in markers are RMS measurements for each respective Fe surface oxidized in air.

NaCl(aq), which can increase electron transfer in the redox reactions. It is known that the Cl^- ions initiate the corrosion by breakdown of the native oxide layer.[54] It should be noted that these experiments are different than the PM-IRRAS experiments, as these measure the surface corrosion in solution in a horizontal orientation (see Figure 1B) without gradual air adsorption. In this way, different information on the physical changes of the surface is obtained in the submerged region of the sample about how the electrolytes affect the surface corrosion.

After *in situ* corrosion experiments using AFM, the samples were rinsed with water and dried in air, allowing for the surface to oxidize from exposure to atmospheric O_2 and CO_2. These measurements were collected just after the liquid imaging on the same day. The RMS roughness measurements in liquid (open markers) are compared to the RMS of the oxidized Fe surfaces (filled in markers) in the same plot, where the markers are shown at a much later time period. Upon oxidation in air, the Fe surface exposed to 5 mM $CaCl_2$(aq) had the highest average RMS roughness value of 77 ± 34 nm, compared to the 5 mM NaCl(aq) that had a corresponding RMS value of 26 ± 9 nm. The RMS values for 5 mM $CaCl_2$(aq) reached the peak roughness value after about 2 h, while the 5 mM NaCl(aq) reached the peak roughness value after about 3 h. This implies that changes in the surface roughness, an estimate of the corrosion rate, on the Fe surface is faster in $CaCl_2$(aq).

3.4.1. Ex Situ AFM Images of Fe Surfaces after Air Oxidation. After the imaging in the electrolytes, the surface was rinsed with nanopure water and oxidized in air (dried) prior to AFM imaging to prevent dragging of loose debris left over from the liquid phase. It should be noted that any product that was not chemically bound to the surface would have been removed during the rinsing process. The *ex situ* AFM images revealed that different types of morphologies resembling minerals were produced from the surface oxidation, as shown in Figure 9. These images were collected from several different concentrations (1, 5, and 10 mM) of both electrolytes that were separately applied to the Fe surface for different lengths of time, as described in the Methods section.

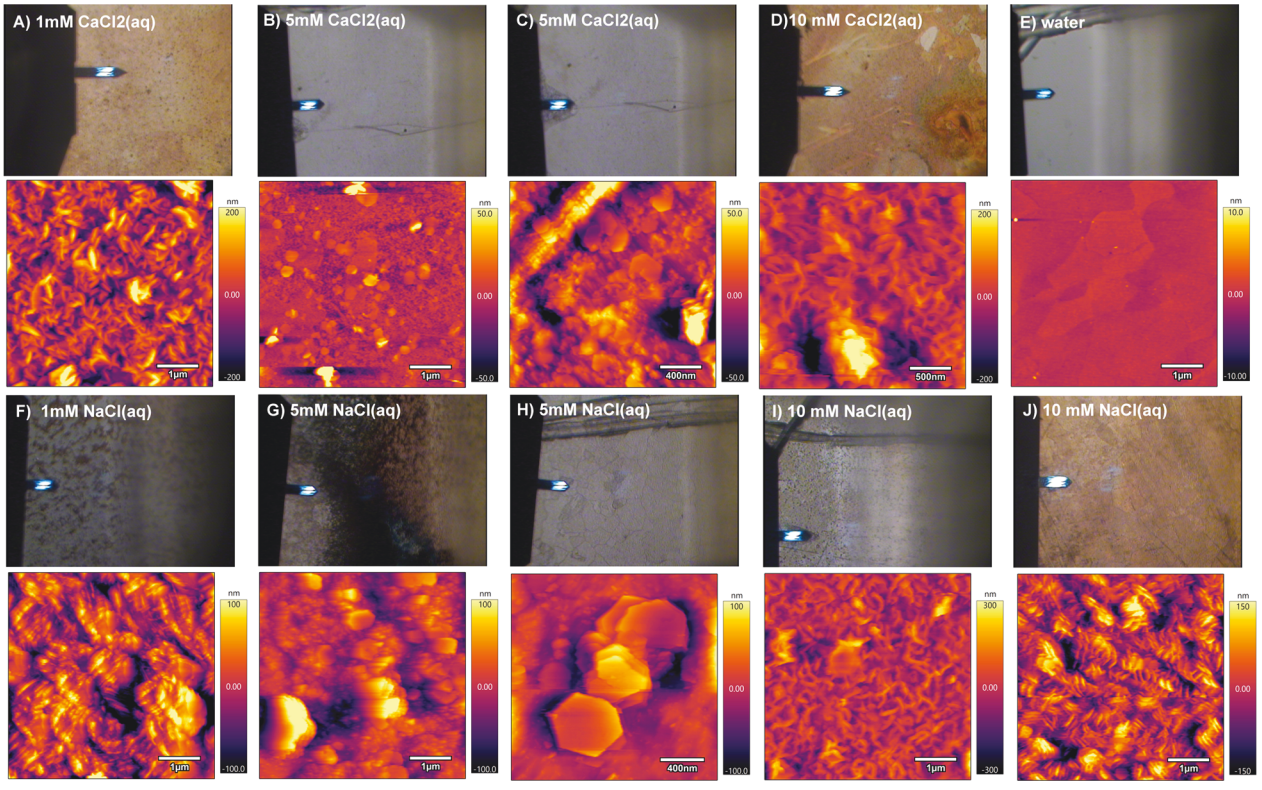

Figure 9. AFM images of Fe after air oxidation after exposed to (A) 1 mM $CaCl_2$(aq), (B,C) 5 mM $CaCl_2$(aq), (D) 10 mM $CaCl_2$(aq), (E) nanopure water, (F) 1 mM NaCl(aq), (G,H) 5 mM NaCl(aq), and (I,J) 10 mM NaCl(aq). Camera images are shown above each AFM image.

https://doi.org/10.1021/acs.jpca.1c06451
J. Phys. Chem. A 2021, 125, 8047−8063

Strand-like features were observed for Fe exposed to 1 mM $CaCl_2$(aq) with dimensions of 200−260 nm in width in Figure 9A. Two separate experiments of the Fe surface exposed to 5 mM $CaCl_2$(aq) produced hexagonal-shaped platelets with diameters ranging between 150 and 360 nm and are observed in Figure 9B,C, resembling features similar to green rust, a double-layered Fe hydroxy carbonate mineral.[43,55−57] Different strand-like features of 120−188 nm in width were observed for the Fe surface exposed to 10 mM $CaCl_2$(aq) in Figure 9D, having similarities to those observed for lepidocrocite.[58,59] The image of the Fe surface in water and dried in air is shown in Figure 9E for comparison, where no features resembling corrosion were observed.

The AFM images in Figure 9F−J show topographical features of corroded Fe after exposure to different concentrations of NaCl(aq). After exposure of Fe to 1 mM NaCl(aq) for 3 h, Figure 9F, elongated grain-like features between 716 and 806 nm in width were observed similarly to features observed for goethite (α-FeOOH).[60] We cannot confirm that goethite was produced on the surface from the ATR−FTIR spectroscopy results in Figure 5. However, AFM is more sensitive to the top layers of the surface changes compared to the depth resolution (several μm) of ATR−FTIR spectroscopy, and it is possible that some goethite may be produced upon air oxidation. Upon exposure of the Fe surface to the higher concentration of 5 mM NaCl(aq) in Figure 9G−H, hexagonal platelets of lengths between 500 and 626 nm in diameter were observed, as resulting corrosion products of the reaction. When the Fe surface was exposed to 10 mM NaCl(aq), Figure 9I,J reveals two distinct morphologies, a strand-like morphology that is similar to lepidocrocite[58,61] and conformal platelets, respectively. The Fe surface was exposed to the 10 mM NaCl(aq) for 2 h and 35 min for 9I and 5 h and 4 min for images in Figure 9J. These results may suggest that the rate of change of surface roughness depends on the electrolyte concentration and exposure time may have an effect on the resulting morphology.

Similar features were observed from the Fe surface exposed to 5 mM $CaCl_2$(aq) or NaCl(aq) in Figure 9B,C,G,H. These hexagonal platelets are similar to a chloride/carbonate species ($Fe_4(OH)_8Cl{\cdot}nH_2O/[Fe_6(OH)_{12}][CO_3{\cdot}nH_2O]$) that has been observed as "green rust".[43,55,56,62,63] In that study, the green rust was observed as an intermediate state that transformed later into Fe oxyhydroxides.[55,63] In our observations, we observe similar morphologies but no evidence of a visible green color on the surface, suggesting that it is possible that we observe an hydroxy carbonate material,[13,64] in agreement with our ATR−FTIR spectra in Figure 5B,D.

The hexagonal platelets produced in Figure 9B,C after exposing the surface to 5 mM $CaCl_2$(aq) are similar to those observed for the Fe surface to exposed to NaCl(aq). The corrosion products observed from the AFM images of Fe exposed to 10 mM $CaCl_2$(aq) show similar features to that of the Fe surface exposed to 10 mM NaCl(aq) (Figure 9I,J). These features presented in the AFM images were observed on a spot on the surface that was fully submerged and exposed to air only after rinsing the solution. Therefore, we can conclude that a heterogeneous mixture of minerals is shown to nucleate on the surface at different stages during the corrosion since different solution concentrations and submersion times were used. These differences in the observations over time are attributed to the fact that the concentration of the solution is related to the corrosion rate, where the higher the solution concentration, and therefore the ionic strength, the higher the conductivity of the electrolyte, the faster the charge transfer, and the faster the corrosion.

During corrosion, multiple pitting events on the surface are created, leading to more dissolution of Fe^{2+}.[12,14] After enough time, the dissolved Fe^{2+} ions aggregate and precipitate out of solution, resulting in corrosion deposition (as shown in the optical images in Figures 7 and 9). This pitting and redeposition of precipitated products at higher concentrations leads to more nucleation sites for crystal growth on the surface. Once the surface was rinsed and exposed to air, the Fe surface oxidizes in the presence of O_2 and CO_2 to produce the morphologies resembling the aforementioned minerals. These are possible explanations for why we observe different morphologies on the surface after corrosion at different solution concentrations.

4. DISCUSSION

In this project, we studied the influence of $CaCl_2$(aq) and NaCl(aq) on Fe surface corrosion at the air/electrolyte/iron interface under ambient conditions using PM-IRRAS to observe the chemical changes. The *ex situ* post analysis of samples using ATR−FTIR spectroscopy, XPS, and AFM also complemented the PM-IRRAS spectra in identifying the composition of corrosion products. The physical changes of the Fe surface corrosion were imaged using AFM in liquid and in air. Based on our observations, we summarize why CO_2 adsorption and mineral formation at the air/electrolyte/Fe interface is different than corrosion on iron surfaces submerged in electrolytes at the liquid/solid interface and how our observations lead to understanding the corrosion mechanism. Below, we propose surface reactions based on our observations that are summarized in the schematic in Figure 10. Some dissolved species, such as O_2, OH^-, and Fe^{2+}, are omitted for simplifying the surface reaction.

In this study, the effect of $CaCl_2$(aq) and NaCl(aq) electrolytes was measured on the surface corrosion of Fe with an emphasis on the role of the cation. Both these electrolytes contain Cl^-, an ion known to catalyze surface corrosion by initiating the pitting events, but different countercations, Ca^{2+} and Na^+. Although their solution concentrations and cation concentrations are the same, there is twice as much chloride in $CaCl_2$(aq) compared to that of NaCl(aq). Therefore, it is expected that the surface roughness would change more rapidly in $CaCl_2$(aq) compared to NaCl(aq). In addition, the 10 mM $CaCl_2$(aq) has more ions and a higher rate of charge transfer, and therefore, $CaCl_2$(aq) was found to have the higher rate of corrosion as measured by surface roughness using AFM.

It is known that the Cl^- leads to pitting of the native oxide film, initiating corrosion of the surface. A higher Cl^- concentration in $CaCl_2$(aq) leads to a higher number of pitting sites on the surface, which act as active sites for corrosion due to local acidification within the pit,[14,65−67] increasing the rate of corrosion,[54] as observed in the *in situ* liquid AFM measurements. Additionally, by increasing electrolyte concentrations, more nucleation sites were produced and subsequent air oxidation of the iron surface resulted in different mineral growth morphologies. This may be dependent on the time the surface was exposed to the electrolyte, other dissolved species in solution, and the concentration of the solution, which affect the rate of corrosion.

https://doi.org/10.1021/acs.jpca.1c06451
J. Phys. Chem. A 2021, 125, 8047−8063

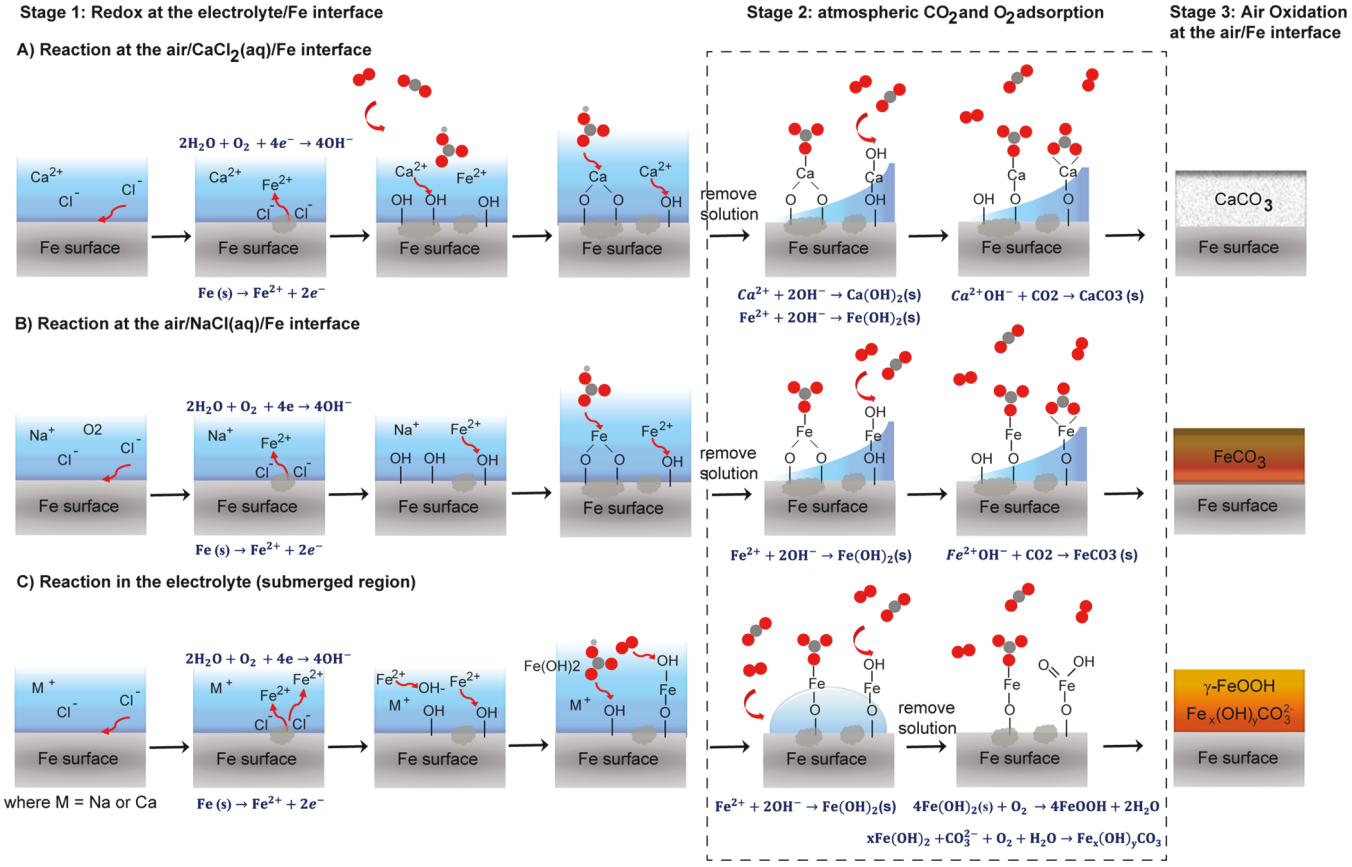

Figure 10. Schematic of the proposed mechanism for iron surface corrosion and mineral growth: (A) $CaCO_3$ is produced at the Fe interface in $CaCl_2$(aq), (B) $FeCO_3$ is produced at the Fe interface in NaCl(aq), and (C) a heterogeneous mixture of γ-FeOOH and an Fe hydroxy carbonate ($Fe_x(OH)_yCO_3$) is produced in the submerged region of the solution. (Red—oxygen, gray—carbon, and light gray—hydrogen). (Image is not drawn to scale.)

After pitting through the native oxide layer into the metallic Fe surface, it is known that the Fe^0 is oxidized to Fe^{2+} (at the anode) and reacts with dissolved OH^- or surface OH^- species (from the cathode reaction of dissolved O_2 and H_2O). The Cl^- also has a high affinity to bind with Fe, producing Fe complexes ($FeCl_2$) that dissolve into solution. These dissolved Fe^{2+} species from the surface affect the topographical changes observed in the AFM images and show that the Fe surface corrodes at different rates, which may depend on the number of ions in solution and the total charge (ionic strength). During corrosion, in the submerged region in Figure 10C (from the AFM images), the higher the concentration of ions of the solution, the higher the conductivity, and this increases the rate of the corrosion as observed in the RMS analysis. Although we cannot directly tie the surface roughness to chemical identity, the ATR−FTIR spectroscopy results show the oxidation of the Fe surface to a heterogeneous mixture of lepidocrocite and an Fe oxyhydroxide carbonate, which does not depend on the cation. This is the initial step for the reaction at the interface and in the submerged regions, as illustrated in row C of Figure 10.

At the air/electrolyte/iron interface, differences in the surface chemistry are observed.

4.1. Interfacial Oxidation of the Fe Surface in $CaCl_2$(aq). In the redox reaction, the Fe^{2+} is created at the anode, with dissolved O_2 and water producing OH^- at the cathode. On the surface, the Fe^0 sites are converted to Fe^{2+} sites upon reaction (as shown in Figure S8) to produce $Fe(OH)_2$, as given in Figure 10A−C. At the air/$CaCl_2$(aq)/Fe interface, we propose that these OH sites easily react with dissolved Ca^{2+} to produce the $Ca(OH)_2$ as an intermediate as observed from the presence of the νCa−O at 711 cm^{-1} in the vibrational spectroscopy results. The resulting $Ca(OH)_2$ is more reactive toward atmospheric CO_2,[37,38,68] as calcium is known for a strong adsorption of CO_2 and used as a natural mineral for CO_2 sequestration technologies.[21,69,70] In stage 2, the electrolyte is removed and the interface region is immediately exposed to air, allowing the sample to oxidize further. In this stage, it is probable that atmospheric CO_2 enters into the ultra-thin meniscus layer, where dissolved HCO_3^- or CO_3^{2-} species reacts with the surface. Since our previous results in nanopure water (see Supporting Information in ref 13) show little presence of surface-adsorbed carbonates, we suggest that the surface carbonates are produced from reaction of surface $Fe(OH)_2$ with the Ca^{2+} ions, allowing for facile HCO_3^- production (pH = 5.4) or direct atmospheric CO_2 adsorption to the Fe interface. After surface carbonate is grown, an insoluble $CaCO_3$(s) film serves as a temporary protective layer, slowing corrosion at the interface. This was observed as a visibly white film at the interface (Figures 1 and 5A) that acts as a physical barrier to further oxidation from O_2(g). This film growth observation is supported by the presence of strong νCO_3 modes of $CaCO_3$ in the PM-IRRAS and ATR−FTIR spectra (at 1420−1450 cm^{-1}). The XPS results also confirmed the presence of calcium and carbonates at the interface region. These results at

https://doi.org/10.1021/acs.jpca.1c06451
J. Phys. Chem. A 2021, 125, 8047−8063

the interface may also suggest that Ca^{2+} has a preference for the air/electrolyte/Fe interface that has a higher adsorption of CO_2 at the interface compared to the region submerged in the electrolyte.

4.2. In the Submerged Region of Fe in $CaCl_2$(aq). The primary surface species observed is γ-FeOOH, lepidocrocite, with a minor composition of an Fe hydroxide carbonate, as observed in the ATR−FTIR spectra in Figure 5B, Table 1, and the AFM images in Figure 9A−D. In the submerged region of the Fe surface, the fundamental corrosion reactions (Figure 10C) initially begin the same as the interfacial reaction. The difference in these results in the region submerged in the electrolyte is that atmospheric CO_2 is not gradually adsorbed onto the surface from the lack of air exposure during the corrosion reaction, as illustrated in Figure 1B. Here, the entrance for atmospheric CO_2 is at the edges of the droplet. Although a small amount of atmospheric CO_2 dissolves in the solution to form HCO_3^- or CO_3^{2-} species and is present in all the solutions, the concentration of them is very low and may not be sufficient for a significant formation of surface carbonate. Here, dissolved O_2 and H_2O play a larger role in the cathodic reaction, in the oxidation and corrosion of the iron surface to γ-FeOOH.

After the $CaCl_2$(aq) electrolyte is removed and the sample is exposed to air, atmospheric CO_2 can react with the already produced γ-FeOOH in the (formerly) submerged region, which may explain the presence of minor carbonate species, as shown in the ATR−FTIR spectroscopy results. Previous studies have shown that the CO_2 uptake onto iron oxides is enhanced by a very thin layer of adsorbed water on the oxides.[38] This may be why the interface, where a thin water film is present and CO_2, can easily dissolve into the ultrathin meniscus film (see Figure 1A), produces CO_3^{2-} or HCO_3^- ions to react with surface hydroxyl species and promote the growth of $CaCO_3$. In this case, the entrance of CO_2 into solution is in the meniscus region (as shown in Figure 1A). However, in the droplet case, the entrance for atmospheric CO_2 is from the sides of the droplet (Figure 1B and video timelapse). When atmospheric CO_2 was exposed to the submerged region in stage 3, in the droplet case or the lower region of the sample submerged in PM-IRRAS experiments, the formation of $CaCO_3$ was suppressed due to the lack of gradual exposure to atmospheric CO_2 or dissolved carbonate ions. This allowed for atmospheric O_2 and CO_2 to react quickly with $Fe(OH)_2$ to produce γ-FeOOH and an Fe hydroxy carbonate species ($Fe_x(OH)_yCO_3$),[56,58,62] as summarized in Figure 10C.

4.3. At the Fe Interface Exposed to NaCl(aq). Surface carbonates are produced for the similar reasons as at the air/$CaCl_2$(aq)/Fe interface from atmospheric O_2 and CO_2 adsorption into the NaCl(aq) electrolyte during oxidation of the surface,[13] shown in Figure 10B. In this case, Na^+ acts as a spectator ion, unlike for Ca^{2+}, and gradual atmospheric CO_2 is adsorbed to the interface region, where either CO_2 or dissolved HCO_3^- or CO_3^{2-} species react with $Fe(OH)_2$ sites to produce $FeCO_3$ (siderite). We can surmise that the Fe^{2+} ion is the more reactive Fe species and contributes to the formation of carbonates and hydroxides. The rate of formation of $FeCO_3$ at the Fe interface is initially slower than the rate of formation for $CaCO_3$ for Fe exposed to $CaCl_2$(aq), as observed from the PM-IRRAS results in Figure 3 and the video timelapse (see Supporting Information and Figure S3), but continues to grow multiple layers during air oxidation after the electrolyte layer is removed.

4.4. In the Submerged Region of Fe Exposed to NaCl(aq). The same lepidocrocite (γ-FeOOH) and the Fe hydroxy carbonate species ($Fe_x(OH)_yCO_3$) were grown as the primary corrosion products, similarly to Fe in $CaCl_2$(aq), from reaction with $Fe(OH)_2$,[43,55] as shown from the same vibrational signatures in the ATR−FTIR spectra (Figure 5B,D). We believe that this is a similar mechanism for Fe in both electrolytes in the submerged region of the solution, as shown in Figure 10C. Evidence of similar features are observed in the AFM images for both electrolyte solutions (Figure 9F−J) after air oxidation, suggesting that the cation identity does not play a role in forming the same minerals in the submerged region of the solution. Additionally, we observed similar features in the AFM images after air oxidation in stage 3 at different electrolyte concentrations, at 1, 5, or 10 mM (Figure 9). This might originate from the rate of pitting increasing at higher concentrations (and higher Cl^-), which leads to more high-surface-area active sites for adsorption of dissolved (CO_3^{2-}, HCO_3^-, and OH^-, O_2) species or upon air exposure, from atmospheric O_2, and CO_2 to form γ-FeOOH and the $Fe_x(OH)_yCO_3$ minerals.

Only at the interface region in the PM-IRRAS experiments at the air/electrolyte/Fe interface, unique carbonate minerals are grown, from gradual exposure of the electrolyte to atmospheric CO_2 and O_2. This also suggests the preference for the Ca^{2+} ions to adsorb at the air/electrolyte interface, which react quickly to form the $CaCO_3$ films in $CaCl_2$(aq) compared to $FeCO_3$ in NaCl(aq), where Na^+ acts as a spectator ion. At the interface, we observe how the cation identity in the electrolyte with atmospheric gases impacts the growth of the carbonate film. Since the $CaCl_2$(aq) has more Cl^- ions and more charge compared to NaCl(aq), corrosion and oxidation occur quickly in $CaCl_2$(aq) but come to a saturation point as observed in the PM-IRRAS coverage analysis and video timelapse (see Supporting Information and Figure S3) recording. In NaCl(aq), the rate of oxidation and mineral growth is gradual and continues beyond the timing observed for $CaCl_2$(aq). These studies demonstrate that the initial stages of corrosion and oxidation in different electrolytes impact the carbonate formation from CO_2 adsorption and influence mineral formation at complex interfaces. Further investigations are needed to measure surface chemistry of how ions and complex interfaces affect fundamental growth processes for reactions in the environment, especially for chemistries impacting surface corrosion, redox processes, and CO_2 capture for sequestration.

5. CONCLUSIONS

The interfacial and atmospheric corrosion of iron was studied under two different electrolytic environments, in $CaCl_2$(aq) and NaCl(aq). The PM-IRRAS spectra of atmospheric O_2(g) and CO_2(g) adsorption and oxidation in air at the iron interface were collected as a function of time. The topographical changes that occur on the iron surface exposed to $CaCl_2$(aq) and NaCl(aq) were monitored using *in situ* AFM liquid imaging and *ex situ* AFM air imaging. The post analysis of corroded iron samples was performed using XPS and ATR−FTIR techniques to confirm the corrosion product and mineral composition.

The *in situ* PM-IRRAS spectra and *ex situ* ATR−FTIR spectra of the air/electrolyte/Fe interface reveal that different

https://doi.org/10.1021/acs.jpca.1c06451
J. Phys. Chem. A 2021, 125, 8047−8063

mineral carbonate films are produced that are unique to the electrolyte composition. At the Fe interface exposed to $CaCl_2$(aq), calcium carbonate ($CaCO_3$) was produced, identified as a combination of aragonite and calcite. When the iron surface was exposed to NaCl(aq) and air, siderite ($FeCO_3$) was produced. This suggests that the insoluble $CaCO_3$ has been deposited on the iron surface, which can act as a temporary protective layer against further oxidation to γ-FeOOH. This protective layer avoids further immediate oxidation from O_2, thus slowing the surface corrosion. Reasons for these unique carbonate films were attributed to Na^+ that acts as a spectator ion and Fe^{2+} that acts as the reacting cation species, producing siderite, while interfacial Ca^{2+} reacts with atmospheric CO_2 or dissolves species to produce the calcite and aragonite layer at the interface.

Similar minerals, lepidocrocite (γ-FeOOH) and a hydroxy carbonate ($Fe_x(OH)_yCO_3$) mineral, were produced on the Fe surface completely submerged in either $CaCl_2$(aq) or NaCl(aq) electrolyte, as identified by ATR−FTIR spectroscopy and XPS. The morphology of the surface changes indicated a heterogeneous mixture of these minerals was grown on the Fe surface, as observed from *ex situ* AFM. These findings were also due to the increased oxidation in solution and the lack of gradual adsorption of carbonate ions or atmospheric CO_2. The surface roughness, an estimate of the corrosion rate, was found to increase with the number of Cl^- ions and total charge in solution, but the same mixture of surface morphologies was produced in both electrolytes. These studies are important toward understanding nucleation and mineral formation by reactions in complex environments and also show that the electrolyte composition highly influences the type of mineral grown.

■ ASSOCIATED CONTENT

Supporting Information

The Supporting Information is available free of charge at https://pubs.acs.org/doi/10.1021/acs.jpca.1c06451.

Raw PM-IRRAS spectra (uncorrected baseline); raw PM-IRRAS spectra of Fe in $CaCl_2$(aq) in D_2O; video timelapse description; images of PM-IRRAS experiments; ATR−FTIR spectra of 10 mM solutions; XPS spectra of the O 1s region of the mineral specimens; XPS spectra of the C 1s region of the mineral specimens; XPS spectra of the Na 1s and Ca 2p region of the corroded samples; XPS spectra of the Fe 2p region of the corroded samples; XPS spectra of the Fe 2p and Ca 2p region of mineral specimens; and Table of the XPS elemental composition of mineral specimens (PDF)

Visual timelapse of corrosion (MP4)

■ AUTHOR INFORMATION

Corresponding Author

Kathryn A. Perrine − *Department of Chemistry, Michigan Technological University, Houghton, Michigan 49931, United States;* orcid.org/0000-0002-5048-6411; Email: kaperrin@mtu.edu

Authors

Chathura de Alwis − *Department of Chemistry, Michigan Technological University, Houghton, Michigan 49931, United States;* orcid.org/0000-0003-1606-2153

Mikhail Trought − *Department of Chemistry, Michigan Technological University, Houghton, Michigan 49931, United States;* orcid.org/0000-0003-0705-782X

Julia Lundeen − *Department of Materials Science & Engineering, Michigan Technological University, Houghton, Michigan 49931, United States*

Complete contact information is available at: https://pubs.acs.org/10.1021/acs.jpca.1c06451

Author Contributions

C.d.A. performed the PM-IRRAS and ATR−FTIR experiments. C.d.A. and K.A.P. interpreted PM-IRRAS, ATR−FTIR, and XPS spectra and wrote the majority of the manuscript. M.T. and J.L. imaged the AFM in liquid and in air. M.T. analyzed the AFM data and scripted the AFM section. J.L. helped conceive the early ideas for the AFM analysis.

Funding

This work was supported by the Michigan Tech 2020 Research Excellence Fund, the Department of Chemistry, and the College of Arts and Sciences at Michigan Technological University and the David J. and Valeria Pruett Graduate Research Fellowship. The AFM instrument was funded by the NSF CHE #1725818. Mineral specimens are loaned, courtesy of the A. E. Seaman Mineral Museum at Michigan Technological University.

Notes

The authors declare no competing financial interest.

■ ACKNOWLEDGMENTS

Parts of this study were completed using Michigan Technological University's Applied Chemical and Morphological Analysis Laboratory (ACMAL). Our gratitude is extended to Danielle Langdon for AFM training and former ACMAL Director Owen P. Mills. We thank Dr. Timothy R. Leftwich for running the XPS analysis on the samples. We acknowledge Katharine Amar-Fox and Daniel Seguin for help with polishing iron samples and access to polishing equipment. Zach Angst and Kayleigh Wahr are acknowledged for AFM imaging of select samples. We also thank Jeff Toorongian for help with compressing the video timelapse frame.

■ ABBREVIATIONS

PM-IRRAS, polarized modulated-infrared reflection absorption spectroscopy; ATR−FTIR, attenuated total reflectance−Fourier transformed infrared; XPS, X-ray photoelectron spectroscopy; AFM, atomic force microscopy; CO_3, carbonate; $CaCO_3$, calcium carbonate; $FeCO_3$, siderite; γ-FeOOH, lepidocrocite; $Fe_x(OH)_yCO_3$, iron hydroxy carbonate

■ REFERENCES

(1) Pieper, K. J.; Tang, M.; Edwards, M. A. Flint Water Crisis Caused By Interrupted Corrosion Control: Investigating "Ground Zero" Home. *Environ. Sci. Technol.* **2017**, *51*, 2007−2014.

(2) Masters, S.; Edwards, M. Increased Lead in Water Associated with Iron Corrosion. *Environ. Eng. Sci.* **2015**, *32*, 361−369.

(3) Trueman, B. F.; Sweet, G. A.; Harding, M. D.; Estabrook, H.; Bishop, D. P.; Gagnon, G. A. Galvanic Corrosion of Lead by Iron (Oxyhydr)Oxides: Potential Impacts on Drinking Water Quality. *Environ. Sci. Technol.* **2017**, *51*, 6812−6820.

(4) Huang, L.-F.; Scully, J. R.; Rondinelli, J. M. Modeling Corrosion with First-Principles Electrochemical Phase Diagrams. *Annu. Rev. Mater. Sci.* **2019**, *49*, 53−77.

(5) Richards, C. S.; Wang, F.; Becker, W. C.; Edwards, M. A. A 21st-Century Perspective on Calcium Carbonate Formation in Potable Water Systems. *Environ. Eng. Sci.* **2018**, *35*, 143−158.
(6) Matamoros-Veloza, A.; Barker, R.; Vargas, S.; Neville, A. Iron Calcium Carbonate Instability: Structural Modification of Siderite Corrosion Films. *ACS Appl. Mater. Interfaces* **2020**, *12*, 49237−49244.
(7) Ren, L.; Cheng, Y.; Wang, Q.; Yang, J. Simulation of the relationship between calcium carbonate fouling and corrosion of iron surface. *Colloids Surf., A* **2019**, *582*, 123882.
(8) Sander, A.; Berghult, B.; Broo, A. E.; Johansson, E. L.; Hedberg, T. Iron corrosion in drinking water distribution systems - The effect of pH, calcium and hydrogen carbonate. *Corros. Sci.* **1996**, *38*, 443−455.
(9) Ahmad, E. A.; Chang, H.-Y.; Al-Kindi, M.; Joshi, G. R.; Cooper, K.; Lindsay, R.; Harrison, N. M. Corrosion Protection through Naturally Occurring Films: New Insights from Iron Carbonate. *ACS Appl. Mater. Interfaces* **2019**, *11*, 33435−33441.
(10) Frankel, G.; Mauzeroll, J.; Thornton, G.; Bluhm, H.; Morrison, J.; Maurice, V.; Rayment, T.; Williams, D.; Cook, A.; Joshi, G.; et al. Corrosion scales and passive films: general discussion. *Faraday Discuss.* **2015**, *180*, 205−232.
(11) Scully, J. R. Future Frontiers in Corrosion Science and Engineering, Part II: Managing the Many Stages of Corrosion. *Corrosion* **2019**, *75*, 123−125.
(12) Frankel, G. S.; Li, T.; Scully, J. R. Localized Corrosion: Passive Film Breakdown vs Pit Growth Stability. *J. Electrochem. Soc.* **2017**, *164*, C180−C181.
(13) de Alwis, C.; Perrine, K. A. In Situ PM-IRRAS at the Air/Electrolyte/Solid Interface Reveals Oxidation of Iron to Distinct Minerals. *J. Phys. Chem. A* **2020**, *124*, 6735−6744.
(14) Soltis, J. Passivity breakdown, pit initiation and propagation of pits in metallic materials - Review. *Corros. Sci.* **2015**, *90*, 5−22.
(15) Song, Y.; Jiang, G.; Chen, Y.; Zhao, P.; Tian, Y. Effects of chloride ions on corrosion of ductile iron and carbon steel in soil environments. *Sci. Rep.* **2017**, *7*, 6865.
(16) Li, R. A.; McDonald, J. A.; Sathasivan, A.; Khan, S. J. Disinfectant residual stability leading to disinfectant decay and by-product formation in drinking water distribution systems: A systematic review. *Water Res.* **2019**, *153*, 335−348.
(17) Wang, H.-b.; Li, Y.; Cheng, G. X.; Wu, W.; Zhang, Y. H.; Li, X. Y. Electrochemical Investigation of Corrosion of Mild Steel in NH_4Cl Solution. *Int. J. Electrochem. Sci.* **2018**, *13*, 5268−5283.
(18) Baltrusaitis, J.; Usher, C. R.; Grassian, V. H. Reactions of sulfur dioxide on calcium carbonate single crystal and particle surfaces at the adsorbed water carbonate interface. *Phys. Chem. Chem. Phys.* **2007**, *9*, 3011−3024.
(19) Prieto, M.; Heberling, F.; Rodríguez-Galán, R. M.; Brandt, F. Crystallization behavior of solid solutions from aqueous solutions: An environmental perspective. *Prog. Cryst. Growth Charact. Mater.* **2016**, *62*, 29−68.
(20) Scully, J. R. Corrosion chemistry closing comments: opportunities in corrosion science facilitated by operando experimental characterization combined with multi-scale computational modelling. *Faraday Discuss.* **2015**, *180*, 577−593.
(21) Kelemen, P. B.; McQueen, N.; Wilcox, J.; Renforth, P.; Dipple, G.; Vankeuren, A. P. Engineered carbon mineralization in ultramafic rocks for CO_2 removal from air: Review and new insights. *Chem. Geol.* **2020**, *550*, 119628.
(22) Debure, M.; Andreazza, P.; Canizarès, A.; Grangeon, S.; Lerouge, C.; Mack, P.; Madé, B.; Simon, P.; Veron, E.; Warmont, F.; et al. Study of Iron-Bearing Dolomite Dissolution at Various Temperatures: Evidence for the Formation of Secondary Nanocrystalline Iron-Rich Phases on the Dolomite Surface. *ACS Earth Space Chem.* **2017**, *1*, 442−454.
(23) Ingham, B.; Ko, M.; Laycock, N.; Burnell, J.; Kappen, P.; Kimpton, J. A.; Williams, D. E. In situ synchrotron X-ray diffraction study of scale formation during CO_2 corrosion of carbon steel in sodium and magnesium chloride solutions. *Corros. Sci.* **2012**, *56*, 96−104.
(24) Sanna, A.; Uibu, M.; Caramanna, G.; Kuusik, R.; Maroto-Valer, M. M. A review of mineral carbonation technologies to sequester CO_2. *Chem. Soc. Rev.* **2014**, *43*, 8049−8080.
(25) Tao, L.; Huang, J.; Dastan, D.; Wang, T.; Li, J.; Yin, X.; Wang, Q. New insight into absorption characteristics of CO2 on the surface of calcite, dolomite, and magnesite. *Appl. Surf. Sci.* **2021**, *540*, 148320.
(26) Lutton, K.; Blades, W. H.; Scully, J. R.; Reinke, P. Influence of Chloride on Nanoscale Electrochemical Passivation Processes. *J. Phys. Chem. C* **2020**, *124*, 9289−9304.
(27) Alexander, J. M.; Grassian, V. H.; Young, M. A.; Kleiber, P. D. Optical properties of selected components of mineral dust aerosol processed with organic acids and humic material. *J. Geophys. Res.: Atmos.* **2015**, *120*, 2437−2452.
(28) Carrico, C. M.; Kus, P.; Rood, M. J.; Quinn, P. K.; Bates, T. S. Mixtures of pollution, dust, sea salt, and volcanic aerosol during ACE-Asia: Radiative properties as a function of relative humidity. *J. Geophys. Res.: Atmos.* **2003**, *108*, 8650.
(29) Fairén, A. G.; Fernández-Remolar, D.; Dohm, J. M.; Baker, V. R.; Amils, R. Inhibition of carbonate synthesis in acidic oceans on early Mars. *Nature* **2004**, *431*, 423−426.
(30) Grassian, V. H. Chemical reactions of nitrogen oxides on the surface of oxide, carbonate, soot, and mineral dust particles: Implications for the chemical balance of the troposphere. *J. Phys. Chem. A* **2002**, *106*, 860−877.
(31) Rubasinghege, G.; Elzey, S.; Baltrusaitis, J.; Jayaweera, P. M.; Grassian, V. H. Reactions on Atmospheric Dust Particles: Surface Photochemistry and Size-Dependent Nanoscale Redox Chemistry. *J. Phys. Chem. Lett.* **2010**, *1*, 1729−1737.
(32) Voelz, J. L.; Johnson, N. W.; Chun, C. L.; Arnold, W. A.; Penn, R. L. Quantitative Dissolution of Environmentally Accessible Iron Residing in Iron-Rich Minerals: A Review. *ACS Earth Space Chem.* **2019**, *3*, 1371−1392.
(33) Nawrocki, J.; Swietlik, J. Analysis of Corrosion Phenomena in Water-pipe Networks. *Ochr. Srodowiska* **2011**, *33*, 27−40.
(34) Mizuno, T. A Role of Chloride Ions in Pitting Corrosion of Iron. *J. Jpn. Inst. Met.* **1986**, *50*, 1009−1016.
(35) de Alwis, C.; Leftwich, T. R.; Perrine, K. A. New Approach to Simultaneous In Situ Measurements of the Air/Liquid/Solid Interface Using PM-IRRAS. *Langmuir* **2020**, *36*, 3404−3414.
(36) Baltrusaitis, J.; Schuttlefield, J.; Zeitler, E.; Grassian, V. H. Carbon dioxide adsorption on oxide nanoparticle surfaces. *Chem. Eng. J.* **2011**, *170*, 471−481.
(37) Baltrusaitis, J.; Jensen, J. H.; Grassian, V. H. FTIR Spectroscopy combined with isotope labeling and quantum chemical calculations to investigate adsorbed bicarbonate formation following reaction of carbon dioxide with surface hydroxyl groups on Fe_2O_3 and Al_2O_3. *J. Phys. Chem. B* **2006**, *110*, 12005−12016.
(38) Baltrusaitis, J.; Grassian, V. H. Surface reactions of carbon dioxide at the adsorbed water-iron oxide interface. *J. Phys. Chem. B* **2005**, *109*, 12227−12230.
(39) Guo, H.; Qin, Z.; Qian, P.; Yu, P.; Cui, S.; Wang, W. Crystallization of aragonite CaCO3 with complex structures. *Adv. Powder Technol.* **2011**, *22*, 777−783.
(40) Raizada, P.; Shandilya, P.; Singh, P.; Thakur, P. Solar light-facilitated oxytetracycline removal from the aqueous phase utilizing a $H_2O_2/ZnWO_4/CaO$ catalytic system. *J. Taibah Univ. Sci.* **2017**, *11*, 689−699.
(41) Hakim, A.; Marliza, T. S.; Abu Tahari, N. M.; Wan Isahak, R. W. N.; Yusop, R. M.; Mohamed Hisham, W. M.; Yarmo, A. M. Studies on CO2 Adsorption and Desorption Properties from Various Types of Iron Oxides (FeO, Fe2O3, and Fe3O4). *Ind. Eng. Chem. Res.* **2016**, *55*, 7888−7897.
(42) Cho, K. A.; Choi, I.; Kim, I. W. Ball Milling to Build the Hybrid Mesocrystals of Ibuprofen and Aragonite. *J. Nanomater.* **2015**, *2015*, 1−9.
(43) Legrand, L.; Maksoub, R.; Sagon, G.; Lecomte, S.; Dallas, J. P.; Chaussé, A. Electroanalytical and kinetic investigations on the carbonate green rust-Fe(III) redox system. *J. Electrochem. Soc.* **2003**, *150*, B45−B51.

https://doi.org/10.1021/acs.jpca.1c06451
J. Phys. Chem. A 2021, 125, 8047−8063

(44) Rosso, J. J.; Hochella, M. F. Natural Iron and Manganese Oxide Samples by XPS. *Surf. Sci. Spectra* **1996**, *4*, 253.
(45) Roychowdhury, T.; Bahr, S.; Dietrich, P.; Meyer, M.; Thissen, A.; Linford, M. R. Calcite ($CaCO_3$), by near-ambient pressure XPS. *Surf. Sci. Spectra* **2019**, *26*, 014025.
(46) Baer, D. R.; Moulder, J. F. High Resolution XPS Spectrum of Calcite ($CaCO_3$). *Surf. Sci. Spectra* **1993**, *2*, 1.
(47) Stoch, J.; Gablankowska-Kukucz, J. The effect of carbonate contaminations on the XPS O 1s band structure in metal oxides. *Surf. Interface Anal.* **1991**, *17*, 165−167.
(48) Mansour, A. N.; Brizzolara, R. A. Characterization of the Surface of α-FeOOH Powder by XPS. *Surf. Sci. Spectra* **1996**, *4*, 357.
(49) Hao, H.; Li, L.; Yuan, Z.; Patra, P.; Somasundaran, P. Adsorption differences of sodium oleate on siderite and hematite. *Miner. Eng.* **2019**, *137*, 10−18.
(50) Ni, M.; Ratner, B. D. Differentiating calcium carbonate polymorphs by surface analysis techniques - an XPS and TOF-SIMS study. *Surf. Interface Anal.* **2008**, *40*, 1356−1361.
(51) Beard, B. C. Fresh Cleaved Single Crystal NaCl, XPS Spectra, Al Source. *Surf. Sci. Spectra* **1993**, *2*, 91−96.
(52) Demri, B.; Muster, D. XPS study of some calcium compounds. *J. Mater. Process. Technol.* **1995**, *55*, 311−314.
(53) Baltrusaitis, J.; Grassian, V. H. Atomic Force Microscopy and X-ray Photoelectron Spectroscopy Study of NO_2 Reactions on $CaCO_3$ (10(1)over-bar4) Surfaces in Humid Environments. *J. Phys. Chem. A* **2012**, *116*, 9001−9009.
(54) McCafferty, E., *Introduction to Corrosion Science*; Springer: New York, 2010.
(55) Legrand, L.; Abdelmoula, M.; Géhin, A.; Chaussé, A.; Génin, J.-M. R. Electrochemical formation of a new Fe(II)-Fe(III) hydroxy-carbonate green rust: characterisation and morphology. *Electrochim. Acta* **2001**, *46*, 1815−1822.
(56) Savoye, S.; Legrand, L.; Sagon, G.; Lecomte, S.; Chausse, A.; Messina, R.; Toulhoat, P. Experimental investigations on iron corrosion products formed in bicarbonate/carbonate containing solutions at 90 degrees C. *Corros. Sci.* **2001**, *43*, 2049−2064.
(57) Legrand, L.; Sagon, G.; Lecomte, S.; Chausse, A.; Messina, R. A Raman and infrared study of a new carbonate green rust obtained by electrochemical way. *Corros. Sci.* **2001**, *43*, 1739−1749.
(58) Yuan, K.; Lee, S. S.; Wang, J.; Sturchio, N. C.; Fenter, P. Templating Growth of a Pseudomorphic Lepidocrocite Microshell at the Calcite-Water Interface. *Chem. Mater.* **2018**, *30*, 700−707.
(59) Morcillo, M.; Chico, B.; Alcántara, J.; Díaz, I.; Wolthuis, R.; de la Fuente, D. SEM/Micro-Raman Characterization of the Morphologies of Marine Atmospheric Corrosion Products Formed on Mild Steel. *J. Electrochem. Soc.* **2016**, *163*, C426−C439.
(60) Liu, H.; Chen, T.; Zou, X.; Qing, C.; Frost, R. L. Thermal treatment of natural goethite: Thermal transformation and physical properties. *Thermochim. Acta* **2013**, *568*, 115−121.
(61) De la Fuente, D.; Alcántara, J.; Chico, B.; Díaz, I.; Jiménez, J. A.; Morcillo, M. Characterisation of rust surfaces formed on mild steel exposed to marine atmospheres using XRD and SEM/Micro-Raman techniques. *Corros. Sci.* **2016**, *110*, 253−264.
(62) Antony, H.; Legrand, L.; Chaussé, A. Carbonate and sulphate green rusts - Mechanisms of oxidation and reduction. *Electrochim. Acta* **2008**, *53*, 7146−7156.
(63) Roh, Y.; Lee, S. Y.; Elless, M. P. Characterization of corrosion products in the permeable reactive barriers. *Environ. Geol.* **2000**, *40*, 184−194.
(64) Barker, R.; Burkle, D.; Charpentier, T.; Thompson, H.; Neville, A. A review of iron carbonate ($FeCO_3$) formation in the oil and gas industry. *Corros. Sci.* **2018**, *142*, 312−341.
(65) DorMohammadi, H.; Pang, Q.; Murkute, P.; Arnadottir, L.; Isgor, O. B. Investigation of chloride-induced depassivation of iron in alkaline media by reactive force field molecular dynamics. *npj Mater. Degrad.* **2019**, *3*, 19.
(66) Xiong, S.; Zhu, Z.; Jing, L. Influence of Cl-ions on the pitting corrosion of boiler water-wall tube and its principle. *Anti-Corros. Methods Mater.* **2012**, *59*, 3−9.
(67) Galvele, J. R. Transport Processes and the Mechanism of Pitting of Metals. *J. Electrochem. Soc.* **1976**, *123*, 464−474.
(68) Baltrusaitis, J.; Schuttlefield, J. D.; Zeitler, E.; Jensen, J. H.; Grassian, V. H. Surface reactions of carbon dioxide at the adsorbed water-oxide interface. *J. Phys. Chem. C* **2007**, *111*, 14870−14880.
(69) Ibrahim, M. H.; El-Naas, M. H.; Benamor, A.; Al-Sobhi, S. S.; Zhang, Z. E. Carbon Mineralization by Reaction with Steel-Making Waste: A Review. *Processes* **2019**, *7*, 115.
(70) Mutch, G. A.; Morandi, S.; Walker, R.; Anderson, J. A.; Vega-Maza, D.; Operti, L.; Cerrato, G. Cation Dependent Carbonate Speciation and the Effect of Water. *J. Phys. Chem. C* **2016**, *120*, 17570−17578.

https://doi.org/10.1021/acs.jpca.1c06451
J. Phys. Chem. A 2021, 125, 8047−8063